








SN 2020jfo: A Short-plateau Type II Supernova from a Low-mass Progenitor

Rishabh Singh Teja^{1,2}, Avinash Singh³, D. K. Sahu¹, G. C. Anupama¹, Brajesh Kumar⁴, and Nayana A. J.¹

¹Indian Institute of Astrophysics, II Block, Koramangala, Bengaluru-560034, Karnataka, India; rishabh.teja@iiap.res.in, rsteja001@gmail.com

²Pondicherry University, R.V. Nagar, Kalapet, Pondicherry-605014, UT of Puducherry, India

³Hiroshima Astrophysical Science Center, Hiroshima University, Higashi-Hiroshima, Hiroshima 739-8526, Japan

⁴Aryabhata Research Institute of Observational Sciences, Manora Peak, Nainital-263001, Uttarakhand, India

Received 2022 January 12; revised 2022 March 22; accepted 2022 March 25; published 2022 May 2

Abstract

We present spectroscopic and photometric observations of the Type IIP supernova, SN 2020jfo, in ultraviolet and optical wavelengths. SN 2020jfo occurred in the spiral galaxy M61 (NGC 4303), with eight observed supernovae in the past 100 yr. SN 2020jfo exhibited a short plateau lasting < 65 days, and achieved a maximum brightness in Vband of $M_V = -17.4 \pm 0.4$ mag at about 8.0 ± 0.5 days since explosion. From the bolometric light curve, we have estimated the mass of ^{56}Ni synthesized in the explosion to be $0.033 \pm 0.006 M_\odot$. The observed spectral features are typical for a Type IIP supernova except for shallow $\text{H}\alpha$ absorption throughout the evolution and the presence of stable ^{58}Ni feature at 7378 \AA , in the nebular phase. Using hydrodynamical modeling in the MESA + STELLA framework, an ejecta mass of $\sim 5 M_\odot$ is estimated. Models also indicate SN 2020jfo could be the result of a red supergiant progenitor with $M_{\text{ZAMS}} \sim 12 M_\odot$. Bolometric light-curve modeling revealed the presence of a secondary radiation source for initial ~ 20 days, which has been attributed to interaction with a circumstellar material of mass $\sim 0.2 M_\odot$, which most likely was ejected due to enhanced mass loss about 20 yr prior to the supernova explosion.

Unified Astronomy Thesaurus concepts: Core-collapse supernovae (304); Type II supernovae (1731); Supernova dynamics (1664); Observational astronomy (1145); Red supergiant stars (1375); Supernovae (1668); Ejecta (453)

Supporting material: data behind figure

1. Introduction

Core-collapse supernovae (CCSNe) are a diverse and heterogeneous class, mainly due to a vast variety and complexity of their possible progenitors, surroundings, and the physics associated with these. Stars exceeding the threshold of $\sim 8 M_\odot$ terminate their lives in these violent explosions injecting recently synthesized elements, which in turn enrich the interstellar medium. During the progenitor's evolution, they develop a degenerate core with an outer envelope surrounding it, and when this core reaches its ‘‘Chandrasekhar mass’’ ($\sim 1.5 M_\odot$), they implode due to gravitational instability (Burrows & Vartanyan 2021). They leave neutron stars (NSs) or black holes as a remnant post-collapse. Various routes have been proposed for such events, viz. electron-capture supernovae (SNe), Fe-core SNe, γ -ray burst SNe, and pair-instability SNe (Janka 2012 and references therein).

The primary classification of SNe is based on the presence of spectral features around optical maximum (Filippenko 1997). SNe with an absence of hydrogen features in their spectra are termed Type I events, whereas Type II events show prominent hydrogen Balmer features in their spectra (Minkowski 1941). Type II events are further classified based on their light curves, as a Type IIP if a plateau phase of constant luminosity is observed and a Type III when the decline from the peak is linear before falling to the tail powered by the radioactive decay. Type IIP SNe are more commonly observed with a definitive plateau of around 100 days, but with varied luminosity, before falling to the radioactive-decay powered tail. In certain events, narrow and strong emission features in

the spectra arise due to the strong interaction of ejecta with the circumstellar material (CSM), hence terming such events as Type IIn. In addition to these, some events, labeled Type IIb, show hydrogen lines initially in their spectra, which weaken in the later phases when strong helium features are visible.

Direct detection of a progenitor (Van Dyk 2017 and references therein) has tightly constrained the mass range of red supergiant (RSG) progenitors of Type IIP SNe. Type IIP SNe, such as the SN 2012aw (Fraser et al. 2012; Van Dyk et al. 2012) and SN 2012ec (Maund et al. 2013), have a directly detected progenitor in archival images that puts a mass limit of $8 \lesssim M/M_\odot \lesssim 17$ (Arcavi 2017; Branch & Wheeler 2017) for the Type IIP progenitors. However, theoretical models predict a much-higher upper limit for the progenitor mass.

Many statistical studies, including both observational (Anderson et al. 2014; Sanders et al. 2015; Valenti et al. 2016; Guti rrez et al. 2017a) and synthetic/hydrodynamical modeling (Eldridge et al. 2018; Hiramatsu et al. 2021a) have shown that Type IIP, IIL, and IIb form a continuous sequence of objects with the plateau or decline depending on the outer hydrogen envelope mass. It has been seen statistically in both types of attempts that the probability of events occurring with a characteristic small plateau of tens of days is relatively low.

Apart from the above-mentioned properties, detecting the presence of CSM around these events has become quite usual. Conspicuous signatures of CSM have been observed in many CCSNe events both in spectra and light curves (Bullivant et al. 2018; Rui et al. 2019; Singh et al. 2019; Jacobson-Gal n et al. 2022; Zhang et al. 2022). RSGs have a significant mass-loss history, and it is intuitive for the CSM to be present (Mauron & Josselin 2011). However, in many cases, the CSM evades from being detected directly (Andrews et al. 2019; Dong et al. 2021). Nonetheless, the heating effects of such hidden CSM are at

times observed in the form of enhanced luminosity (Nagao et al. 2020; Haynie & Piro 2021).

Even with a robust and ever-increasing classification scheme for these phenomena, some do not fit very well in either one of the classified designations. With the mushrooming SN numbers discovered by the various existing regular night-sky surveys and those expected from forthcoming survey projects, there will be more discrete events that would not be considered standard. Hence, studying the individual events in detail with an endeavour to learn about their origins would help significantly in understanding the classes as a whole.

SN 2020jfo (also known as ZTF20aaynrh) was discovered by Zwicky Transient Facility (ZTF; Bellm et al. 2019), using the Palomar 1.2 m Oschin telescope on 2020 May 06 (JD = 2,458,975.70) in the galaxy M61 (NGC 4303) at $\alpha = 12^{\text{h}}21^{\text{m}}50^{\text{s}}.479$, $\delta = +04^{\circ}28'54''.14$ (J2000). It was discovered at an AB magnitude of 16.0 mag in ZTF-*r*band. Merely within a day after the discovery, spectroscopic classification of SN 2020jfo was performed by the ZTF group (Perley et al. 2020) using spectra obtained with LT/SPRAT, NOT/ALFOSC, and P60/SEDM. Cross-correlation of the observed spectra with the SNID (Blondin & Tonry 2007) library showed a good match to Type IIP SN 1999gi, about 7 days before maximum light. SN 2020jfo was suggested to be a young Type II SN. Based on nebular spectra, Sollerman et al. (2021) suggest the SN to have a low-mass progenitor.

In this paper, we present a comprehensive photometric and spectroscopic analysis along with hydrodynamical modeling of SN 2020jfo. Subsequent sections are divided in the following manner. Section 2 describes optical observations of SN 2020jfo along with a brief outline of the data reduction procedure. Host galaxy properties, light-curve analysis, and various physical parameters of SN 2020jfo are presented in Section 3. Section 4 deals with the spectroscopic properties, while a possible progenitor and its properties estimated using various methods, viz. semi-analytical modeling, nebular-phase spectrum, and hydrodynamical modeling are discussed in Section 5. Section 6 provides a brief summary of the results presented.

2. Observations and Data Reduction

2.1. Optical Photometry with 2 m HCT

A quick follow-up of SN 2020jfo began on 2020 May 07 (JD 2,458,977.2), i.e., ~ 2 days after discovery, with the Himalayan Faint Object Spectrograph Camera (HFOSC; Prabhu 2014) mounted on the 2-m Himalayan Chandra Telescope (HCT), situated at the Indian Astronomical Observatory (IAO), Hanle, India. It was monitored in two phases. In the first phase, it was observed until 2020 July 14 (JD 2,459,044.1), after which it went into solar conjunction. When it reappeared in the night sky, the second phase of observations was carried out from 2020 November 14 (JD 2,459,241.5) to 2021 January 26 (JD 2459241.5). Broadband photometric observations in Bessell *UBVRI* filters were carried out for a total of 23 epochs. The HCT optical data presented here are supplemented with data from the ZTF in *g* and *r* bands, obtained through ALeRCE (Sánchez-Sález et al. 2021).

HFOSC is equipped with an E2V CCD chip having a dimension of 2048×4096 pixels. The readout noise and gain of the camera are $5.75 e^-$ and $0.28 e^- \text{ADU}^{-1}$, respectively. The central $2K \times 2K$ pixels used for imaging, covers a field of view of $10' \times 10'$ at an image scale of $0''.296 \text{ pixel}^{-1}$. Object frames were obtained in multiple filters. In addition to the

object frames, several bias and sky flat frames were observed at each epoch. The data were preprocessed by performing the standard tasks of bias subtraction, flat-fielding, and cosmic ray removal through packages available in IRAF implemented through pyRAF as given in Singh (2021). At certain epochs, especially during the late phase, multiple frames in the same band were observed, which were later aligned and combined to improve the signal-to-noise ratio in the resultant object frame. The zero-points used to calibrate the secondary standards in the SN field were determined using the average color terms for the telescope detector system and field stars calibrated from SN 2014dt field (Singh et al. 2018b).

Since SN 2020jfo is situated in an outer spiral arm of M61, the host brightness could significantly affect the SN luminosity, especially during the late phase. Hence, we used template images of the host, obtained as a part of our monitoring program of SN 2008in, to remove the contribution from the host. The template images were aligned with the field of SN 2020jfo, background subtracted, PSF-matched, and scaled. The scaled templates were then subtracted, leaving only the SN in the resultant images. Aperture photometry of the SN was then performed, and the SN magnitudes were calibrated using the nightly zero-points obtained from the original images. The template subtraction procedure adopted is given in Singh et al. (2019). The estimated magnitudes are listed in Table 1 and plotted in Figure 2.

2.2. UV-optical Photometry with Swift/UVOT

The Neil Gehrels Swift Observatory (Gehrels et al. 2004) database indicated that SN 2020jfo was observed with the Ultra Violet Optical Telescope (UVOT; Roming et al. 2005) on board Neil Gehrels Swift Observatory (Gehrels et al. 2004) in the *UVW2*, *UVM2*, *UVW1*, *UVU*, *UVB*, and *UVV* bands starting from 2020 May 07 (JD 2,458,976.6) and continued until 2020 August 08 (JD 2,459,069.6). The openly accessible archival images⁵ were reduced using packages available via High Energy Astrophysics Software (HEASOFT, v6.27) and with the latest calibration database for the UVOT instrument, following the methods as described in Poole et al. (2008), and Brown et al. (2009). The SN magnitude was extracted using UVOTSOURCE task with an aperture size of 5 arcsec for the source and a similar aperture size to extract the background counts. The final UVOT magnitudes (see Figure 2) were obtained in the Vega system and are tabulated in Table 2. Template subtraction for UVOT images was performed using the mean background flux estimated at the SN 2020jfo location from the archival images of M61 obtained during follow-up of SN 2014dt. A similar flux was also obtained at the SN location as the light curve in the UV filters (*UVW2*, *UVM2*, and *UVW1*) flattened out during the post-plateau phase ($\gtrsim 60$ days).

2.3. Optical Spectroscopy

Spectroscopic observations of SN 2020jfo were primarily carried out with the HCT starting from 2020 May 07 (JD 2,458,977.1) to 2021 January 26 (JD 2,459,241.4), using HFOSC with grisms Gr7 and Gr8. One spectrum at the nebular phase was obtained on 2021 February 21 (JD 2,459,266.5) with the ADFOSC instrument mounted at the 3.6 m Devasthal Optical Telescope (DOT; Omar et al. 2019; Sagar et al. 2019). Standard IRAF packages were used to extract, reduce, and

⁵ <https://www.swift.ac.uk/>

Table 1
Optical Photometry of SN 2020jfo from HCT

JD (2458900+)	Phase (day)	<i>U</i> (mag)	<i>B</i> (mag)	<i>V</i> (mag)	<i>R</i> (mag)	<i>I</i> (mag)
77.2	3.2	13.89 ± 0.17	14.63 ± 0.05	14.85 ± 0.05	...	14.84 ± 0.01
78.3	4.3	...	14.57 ± 0.02	14.80 ± 0.03	14.74 ± 0.07	14.68 ± 0.02
79.2	5.2	...	14.51 ± 0.03	14.61 ± 0.04	14.57 ± 0.04	14.48 ± 0.05
80.2	6.2	13.84 ± 0.08	14.55 ± 0.03	14.61 ± 0.03	...	14.34 ± 0.05
81.1	7.1	13.85 ± 0.02	14.57 ± 0.02	...	14.32 ± 0.05	...
83.1	9.1	...	14.57 ± 0.01	14.59 ± 0.01	14.38 ± 0.02	14.36 ± 0.03
85.1	11.1	14.09 ± 0.05	14.63 ± 0.01	14.57 ± 0.02	...	14.39 ± 0.02
86.1	12.1	...	14.55 ± 0.03	...	-	14.30 ± 0.03
87.1	13.1	...	14.72 ± 0.02	...	14.46 ± 0.04	...
89.3	15.3	14.41 ± 0.07	14.80 ± 0.02	14.70 ± 0.03	14.42 ± 0.02	14.36 ± 0.03
90.2	16.2	14.54 ± 0.06	14.84 ± 0.02	...	14.47 ± 0.04	...
100.2	26.2	15.64 ± 0.11	15.35 ± 0.03	14.80 ± 0.03	14.47 ± 0.03	...
102.3	28.3	15.66 ± 0.13	15.47 ± 0.05	14.80 ± 0.05	14.50 ± 0.02	14.35 ± 0.03
104.3	30.3	...	15.57 ± 0.04	14.82 ± 0.02	14.51 ± 0.02	14.33 ± 0.14
109.2	35.2	16.28 ± 0.11	15.69 ± 0.02	14.86 ± 0.02	14.54 ± 0.02	14.35 ± 0.02
111.1	37.1	16.46 ± 0.06	15.70 ± 0.01	14.91 ± 0.02	14.53 ± 0.03	14.36 ± 0.04
119.2	45.2	16.77 ± 0.13	15.96 ± 0.03	15.01 ± 0.02	14.62 ± 0.05	14.40 ± 0.03
130.2	56.2	...	16.36 ± 0.04	15.20 ± 0.03	14.79 ± 0.03	14.51 ± 0.02
144.2	70.2	19.04 ± 0.14	18.15 ± 0.03	16.90 ± 0.01	16.14 ± 0.02	15.89 ± 0.04
267.5	193.5	...	19.50 ± 0.07	18.67 ± 0.03	17.71 ± 0.06	17.54 ± 0.04
280.5	206.5	...	19.51 ± 0.02	18.71 ± 0.04	17.92 ± 0.02	17.85 ± 0.05
309.5	235.5	...	19.75 ± 0.04	19.21 ± 0.03	18.40 ± 0.04	18.36 ± 0.01
316.4	242.4	...	19.50 ± 0.49	19.48 ± 0.29	18.46 ± 0.17	18.55 ± 0.26
341.4	267.4	19.71 ± 0.05	18.93 ± 0.04	...

Table 2
UV-optical Photometry of SN 2020jfo from Swift/UVOT

JD (2458900+)	Phase (day)	<i>UVW2</i> (mag)	<i>UVM2</i> (mag)	<i>UVW1</i> (mag)	<i>UVU</i> (mag)	<i>UVB</i> (mag)	<i>UVV</i> (mag)
76.6	2.6	12.78 ± 0.02	12.84 ± 0.03	12.92 ± 0.03	13.54 ± 0.03	14.87 ± 0.03	14.93 ± 0.05
79.9	5.9	13.39 ± 0.03	13.17 ± 0.03	13.11 ± 0.03	13.38 ± 0.03	14.61 ± 0.03	14.53 ± 0.05
80.7	6.7	13.76 ± 0.03	13.44 ± 0.03	13.22 ± 0.03	13.39 ± 0.03	14.62 ± 0.03	14.43 ± 0.04
82.1	8.1	14.34 ± 0.04	13.98 ± 0.04	13.56 ± 0.04	13.49 ± 0.04	14.75 ± 0.04	14.54 ± 0.07
86.2	12.2	15.35 ± 0.07	15.20 ± 0.06	14.52 ± 0.05	13.84 ± 0.04	14.82 ± 0.05	14.69 ± 0.07
94.4	20.4	17.60 ± 0.13	17.63 ± 0.12	16.34 ± 0.09	15.16 ± 0.06	15.06 ± 0.04	14.59 ± 0.05
96.0	22.0	17.55 ± 0.13	17.90 ± 0.13	16.64 ± 0.11	15.57 ± 0.07	15.14 ± 0.04	14.63 ± 0.06
103.0	29.0	18.59 ± 0.17	17.43 ± 0.14	17.81 ± 0.18	16.29 ± 0.09	15.54 ± 0.05	14.73 ± 0.06
107.5	33.5	18.05 ± 0.17	...	17.89 ± 0.19	16.48 ± 0.10	15.72 ± 0.06	14.71 ± 0.06
112.7	38.7	18.72 ± 0.20	18.16 ± 0.14	18.04 ± 0.21	17.11 ± 0.15	15.79 ± 0.06	14.92 ± 0.06
118.5	44.5	...	18.50 ± 0.20	17.94 ± 0.23	17.70 ± 0.22	16.04 ± 0.07	14.90 ± 0.07
148.5	74.5	20.31 ± 0.21	17.27 ± 0.26
159.5	85.5	17.08 ± 0.22
164.5	90.5	17.18 ± 0.23
169.6	95.6	17.23 ± 0.50

calibrate the spectra obtained with both the instruments. Details of the reduction procedure are mentioned in Singh et al. (2018a). The spectra of SN 2020jfo were corrected for the host redshift using $z = 0.00502$ (Perley et al. 2020). Log of spectroscopic observations is provided in Table 3.

3. Analysis

3.1. Reddening, Distance, and Metallicity

The Milky Way line-of-sight reddening for M61 is $E(B - V)_{\text{MW}} = 0.0194 \pm 0.0001$ mag, which is obtained from IRSA⁶ Galactic Dust Reddening and Extinction map (Schlafly & Finkbeiner 2011). We also noted a prominent host

NaID absorption with an equivalent width (EW) of 1.14 ± 0.04 Å, in the co-added spectrum obtained from three early phase spectra, spanning 11 to 15 days from the date of explosion (see Section 3.2 for explosion epoch). Here, we have adopted two independent methods to estimate the host galaxy reddening ($E(B - V)_{\text{host}}$). The empirical relations between $E(B - V)$ and the equivalent width of NaID absorption lines provided by Barbon et al. (1990) and Poznanski et al. (2012) were used to infer $E(B - V)_{\text{host}}$ of 0.29 ± 0.01 mag and 0.30 ± 0.08 mag, respectively. Second, the reddening was also estimated using Balmer decrements, with host galaxy spectra from three regions, marked in Figure 1, obtained from the Sloan Digital Sky Survey (SDSS) archive (Ahumada et al. 2020). The ratio of H α and H β line fluxes were measured, and the color excess was estimated using the relation given by Domínguez et al. (2013), which

⁶ NASA/IPAC Infrared Space Archive

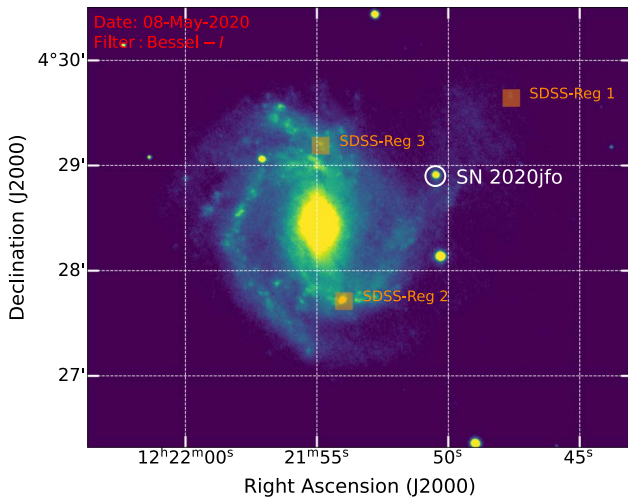


Figure 1. The *I*-band image of SN 2020jfo in M61 obtained on 2020 May 08. The positions of the three regions of the archival SDSS-spectra [dark orange squares] along with SN 2020jfo [white circle] have been marked.

Table 3
Log of Spectroscopic Observations of SN 2020jfo

JD (2458900+)	Phase (day)	Wavelength (Å)
77.1	3	4000–8000; 5200–9000
78.3	4	4000–8000; 5200–9000
79.2	5	4000–8000; 5200–9000
81.2	7	4000–8000; 5200–9000
85.1	11	4000–8000; 5200–9000
86.2	12	4000–8000; 5200–9000
89.3	15	4000–8000; 5200–9000
102.2	28	4000–8000; 5200–9000
110.1	36	4000–8000; 5200–9000
112.1	38	4000–8000; 5200–9000
119.2	45	4000–8000; 5200–9000
129.2	55	4000–8000; 5200–9000
144.1	70	4000–8000
270.5	196	4000–8000
276.5	202	4000–8000; 5200–9000
309.4	235	4000–8000; 5200–9000
341.4	267	4000–8000; 5200–9000
366.4	292	4000–9000 [DOT]

resulted in $E(B - V)_{\text{host}} = 0.25 \pm 0.02$ mag. The reddening estimated using the two independent methods agrees within errors. A weighted mean from the above estimates results in $E(B - V)_{\text{host}} = 0.27 \pm 0.08$ mag. A total reddening of $E(B - V) = 0.29$ mag is adopted throughout this work.

A plethora of distance estimates to the host galaxy M61 are available on the NASA/IPAC Extragalactic Database (NED),⁷ ranging from 7.59 Mpc (Bottinelli et al. 1984) to 35.50 Mpc (Sparks 1994) including both redshift-dependent and redshift-independent measurements. Recent redshift-independent measurements based on SN 2008in constrain the distance from 12–20 Mpc (see Rodríguez et al. 2014; Bose & Kumar 2014). A simple mean of all these estimates could not be adopted as the values are not continuous but at extremes. Steer (2020) has defined a robust method to get enhanced mean estimate

Table 4

O3N2-index and $E(B - V)$ Estimated from the SDSS Spectra of Three Regions in M 61. The regions have been marked in Figure 1

Regions	O3N2-index	12+log[O/H]	$E(B - V)$
SDSS-Reg 1	1.16	8.36	0.28
SDSS-Reg 2	-0.32	8.83	0.22
SDSS-Reg 3	-0.48	8.88	0.26

distances (MED) using the weighted mean for the distances from various primary and secondary sources. From the various means, we have estimated MED 7, which is a combination of the unweighted (MED 2), error-weighted (MED 3), and date-weighted (MED 4) means with weights of 1:2:4, respectively. The distance obtained is $D_L = 16.45 \pm 2.69$ Mpc ($\mu = 31.08 \pm 0.36$ mag).

To estimate the host environment properties, we used archival SDSS spectra of the three regions in M61, as indicated earlier (refer Figure 1). Fluxes of the strong emission lines, viz. $H\alpha$, $H\beta$, $[\text{N II}] 6584 \text{ \AA}$, and $[\text{O III}] 5007 \text{ \AA}$ were measured, and the O3N2 index as prescribed by Pettini & Pagel (2004) was estimated. The gas-phase oxygen abundance ($12 + \log[\text{O}/\text{H}]$) was computed using the relation given in Pettini & Pagel (2004). The metallicity estimates for all three regions are listed in Table 4. We find that toward, the outer edge of the galaxy, the metallicity is subsolar with an oxygen abundance of ~ 8.36 dex ($\sim 0.5 Z_{\odot}$),⁸ whereas in the regions on the spiral arms (Regions 2 and 3), the metallicity is 8.83 dex and 8.88 dex ($\sim 1.6 Z_{\odot}$), respectively.

3.2. Light and Color Curves Evolution

The last nondetection of SN 2020jfo was on UT 2020 May 02.27 (JD 2,458,971.8) with a limiting AB magnitude of 19.7 mag in the *g*-band ZTF filter (Nordin et al. 2020). The SN was discovered on UT 2020 May 06.26 (JD 2,458,975.7). The mid epoch between the last nondetection and the first detection is JD 2,458,973.75. Hence, JD 2,458,974 \pm 2 is taken as the date of explosion and has been used to define the phase throughout this work.

The light-curve evolution of SN 2020jfo in Bessell *U*, *B*, *V*, *R*, *I*, the ZTF-*g*, *-r* bands and in Swift/UVOT bands is shown in Figure 2. Optical light curves show a relatively fast rise to the maximum in all bands. To estimate peak magnitudes and rise times to the peak in various bands, we fitted a cubic spline to the observed photometric data. The estimated peak magnitude and date of maximum in different bands are given in Table 5. The rise time ranges from 5.2 days in *U* to 9.1 days in *R* band, with a similar trend seen in Swift/UVOT bands from 5.7 days in *UVU* to 8.0 days in *UVV*, and 7.1 days and 8.9 days in ZTF-*g* and *-r* bands, respectively. Early phase light curves show a bump around the maximum that is prominent in the redder bands (*R* and ZTF-*r*). Post peak, the light curves vary very slowly in the redder bands and settle onto a plateau, which appears to be short.

To have a better estimate of the plateau length, observations during the transition from plateau to late-declining phase are required. Unfortunately, only one observation could be made during this phase due to observational constraints; however, we notice a steep decline in ZTF-*g* band at +60 days. Moreover,

⁸ Solar value for $12 + \log[\text{O}/\text{H}]$ is taken from Asplund et al. (2006), which is 8.66 ± 0.05 dex.

⁷ <http://ned.ipac.caltech.edu/>

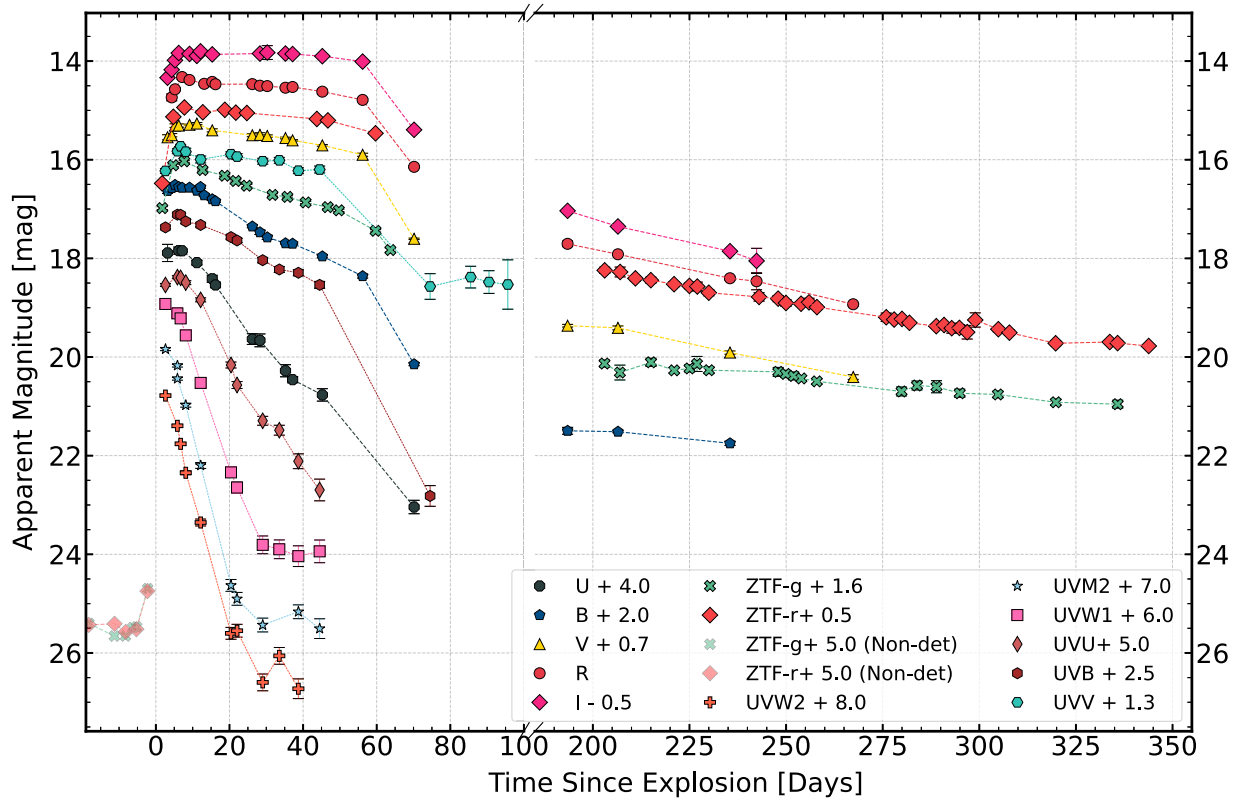


Figure 2. Panchromatic light curves for SN 2020jfo with photometry from HCT, Swift/UVOT, and ZTF. The time period for which SN 2020jfo went behind the Sun has been obliterated from the plot and is marked by the discontinuity in the abscissa. Offsets in the apparent magnitudes are for visual clarity.

Table 5
Peak Magnitudes from UV/Optical Light Curves

Band	$t(m_{\max})$ (MJD)	m_{\max} (mag)
<i>U</i>	$58,978.71 \pm 0.70$	13.83 ± 0.08
<i>B</i>	$58,979.19 \pm 0.28$	14.53 ± 0.03
<i>V</i>	$58,981.54 \pm 0.35$	14.55 ± 0.03
<i>R</i>	$58,982.58 \pm 0.25$	14.38 ± 0.02
<i>I</i>	$58,981.31 \pm 0.56$	14.30 ± 0.05
ZTF- <i>g</i>	$58,980.63 \pm 0.21$	14.46 ± 0.02
ZTF- <i>r</i>	$58,982.35 \pm 0.37$	14.47 ± 0.03
UVU	$58,979.23 \pm 0.28$	13.37 ± 0.03
UVB	$58,980.23 \pm 0.31$	14.61 ± 0.03
UVV	$58,981.54 \pm 0.58$	14.45 ± 0.05

observations around +70 days and beyond (in *UVV*) indicate that the SN has already entered into the radioactive decay tail. This puts an upper limit on the length of the plateau to be 70 days. Also, we do not see any change in slope in the *V*-band light curve until +56 days. With this the lower limit of the plateau length is constrained as 56 days. With these limits, the plateau (OPTd; Anderson et al. 2014) length is estimated as $\approx 63 \pm 7$ days.

Another way to estimate the upper limit of the plateau length is by estimating the date of inflection during the transition phase, which is defined as the point of maximum steepness/slope. We use the formulation from Elmhamdi et al. (2003b) to fit the late-plateau and radioactive decay phase of the *V*-band light curve (Figure 3). We could include some more points in *V*

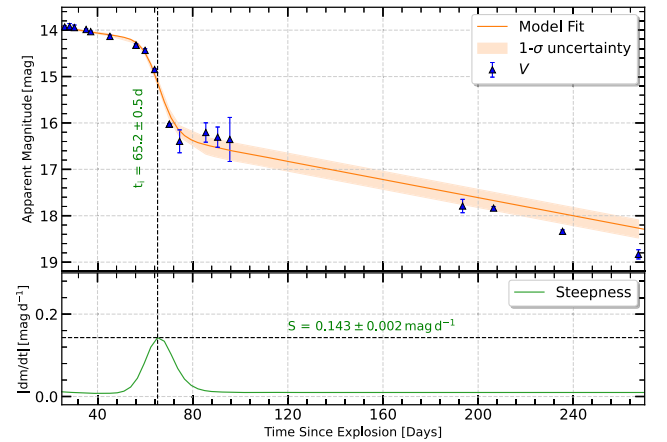


Figure 3. Estimated steepness of SN 2020jfo using the functional form from Elmhamdi et al. (2003b).

band during the transition from plateau to nebular phase using ZTF-*g* and *UVV* magnitudes. The *g*-band magnitudes were transformed to *V* magnitudes using the transformation relations given by Jester et al. (2005). Fit to the better-sampled *V*-band light curve yields a steepness parameter of 0.143 ± 0.002 mag day⁻¹ and day of inflection as 65.2 ± 0.5 days. This is in concurrence with our plateau length estimate.

The mean plateau length for a large sample of Type IIP SNe was found to be ~ 100 days (Anderson et al. 2014), while the estimated plateau length is much shorter, ~ 63 days for SN 2020jfo. Only a handful of such objects have been discovered until now, namely, SN 2006Y, SN 2006ai, SN 2008bp, SN 2008bu (Anderson et al. 2014), SN 2014G

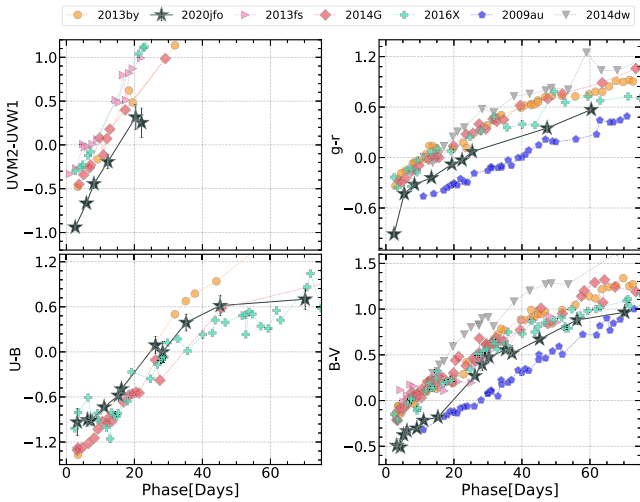


Figure 4. Color evolution of SN 2020jfo from the early rise up to the plateau phase is plotted along with some other Type II SNe.

(Terreran et al. 2016), and SN 2016gez (Hiramatsu et al. 2021a). In a recent study, Hiramatsu et al. (2021a) estimated that only a small fraction ($\sim 4\%$, (3/78)) of short-plateau objects were there in a large sample of Type II SNe studied by Gutiérrez et al. (2018). The rarity of short-plateau objects could also be seen in the Supernova lightCURVE POPulation Synthesis by Eldridge et al. (2018; CURVEPOPS) for Type II SN, as they obtained a mere 4.7% short-plateau Type IIP events out of their 637 models.

Temporal evolution of $UVW2 - UVM2$, $g - r$, $U - B$, and $B - V$ colors for SN 2020jfo, during the early phase is shown in Figure 4. The colors have been corrected for reddening estimated in Section 3.1. The color evolution of some other well-studied objects is also plotted in the same figure for comparison. The color evolution of SN 2020jfo follows the blue to red trend, indicating cooling of the ejecta as the SN evolves. SN 2020jfo shows overall bluer color; the $UVM2 - UVW1$, $B - V$, and $g - r$ color of SN 2020jfo is bluer than all other SN used for comparison, with the exception of SN 2009au.

3.3. Absolute V-band Light Curve

The absolute V-band light curve of SN 2020jfo is obtained after correcting the observed V-band magnitude for extinction and distance estimated in Section 3.1 and $R_V = 3.1$ (Cardelli et al. 1989). The V-band light curve peaked on ~ 8.0 days (JD 2,458,982.04 \pm 0.35) after explosion with an absolute magnitude, $M_V = -17.40 \pm 0.37$ mag. This puts it under the category of luminous Type IIP events. We estimated the light-curve slopes during different phases s_1 , s_2 , and s_3 , (Anderson et al. 2014) for SN 2020jfo as $1.4^{+0.5}_{-0.6}$, $1.5^{+0.4}_{-0.3}$ and $1.6^{+0.2}_{-0.2}$ mag per 100 days, respectively. Based on a large sample of Type II SNe light curves, Anderson et al. (2014) estimate mean values of 2.65 (s_1), 1.23 (s_2), and 1.47 (s_3) mag per 100 days, indicating a clear transition from the early decline to the plateau phase. The estimated values of s_1 and s_2 in the case of SN 2020jfo indicate the absence of such a clear transition, although the rise to maximum is similar to other Type II SNe. It thus appears that the s_1 phase either lasted for a very short period or is missing entirely.

The comparison of V-band absolute-magnitude light curve of SN 2020jfo with other Type II SNe including short-plateau

events is shown in Figure 5. As the number of short-plateau objects studied in detail so far is small, we compared the light curve of SN 2020jfo with a sample of objects including archetypal Type IIP SNe, SN 1999em (Elmhamdi et al. 2003a), and SN 2004et (Sahu et al. 2006); Type II SNe with CSM-signatures, SN 2009au (Rodríguez et al. 2020), SN 2013fs (Bullivant et al. 2018), and SN 2014G (Terreran et al. 2016); and faster declining or short-plateau Type II SNe, SN 2013by (Valenti et al. 2015), SN 2014dw (Valenti et al. 2016), and SN 2016X (Huang et al. 2018). Although SN 2014G and SN 2013by are brighter than SN 2020jfo during the premaximum, early decline, and plateau phase, whereas in the nebular phase their light curve merges with that of SN 2020jfo. In the case of SN 2013fs, the early postmaximum decline is faster in comparison to SN 2020jfo, but the plateau brightness is similar.

3.4. Quasi-bolometric Light Curve

The quasi-bolometric light curve (Q-bol) of SN 2020jfo is estimated using the observed magnitudes in $UVW2$, $UVM2$, $UVW1$, U , B , ZTF-g, V , R , and I filters, corrected for reddening due to the Milky Way and the host galaxy. Extinction corrections in individual photometric bands are applied using the relations by Cardelli et al. (1989 $R_V = 3.1$). The extinction-corrected apparent magnitudes were converted to monochromatic fluxes at the effective filter wavelength, using the magnitude-to-flux conversion zero-points listed in Bessell et al. (1998). Zero-point for bands other than Bessell U , B , V , R , I filters were taken from the Spanish Virtual Observatory (SVO) Filter Profile Service.⁹ The spectral energy distribution (SED) curve for each epoch was estimated by interpolating the estimated flux in different bands using a Cubic spline. Finally, the quasi-bolometric flux was estimated by integrating the SED through the initial wavelength of the first band to the upper cutoff wavelength of the last band. On the nights when magnitudes were not available for some bands, we used linear interpolation to estimate them.

The quasi-bolometric luminosity for initial epochs, i.e., up to +28 days, includes UV fluxes obtained from Swift/UVOT, and beyond that, the contribution is computed only using $UBgVRI$ filters. Figure 6 shows the quasi-bolometric light curve with and without UV contribution. It is evident from Figure 6 (and its inset) that during the first ~ 15 days, contribution from UV bands to the bolometric flux is significant, and beyond this, it becomes very small in comparison to the optical flux. During the late-nebular phase, where only ZTF data are available, the bolometric correction (BC_g) was derived using the last few points in the light curve for which the $BgVRI$ bolometric luminosity could be obtained. The estimated BC_g was applied to ZTF-g-band magnitudes to obtain the bolometric luminosity until the very late phase.

For comparing our bolometric estimates, we also use SuperBol (Nicholl 2018), with ZTF-g as the reference band. SuperBol fits a polynomial to bands with missing data and integrates those at epochs of the reference band. It seems to slightly underestimate the luminosity at the earlier epochs, where we see some signs of enhanced flux in individual optical light curves. It might be due to the smoothing of the data with a polynomial approximation. At other phases, the quasi-bolometric light flux estimated in two different ways matches quite well. The contribution from optical flux to the UV+Optical

⁹ <http://svo2.cab.inta-csic.es/theory/fps/>

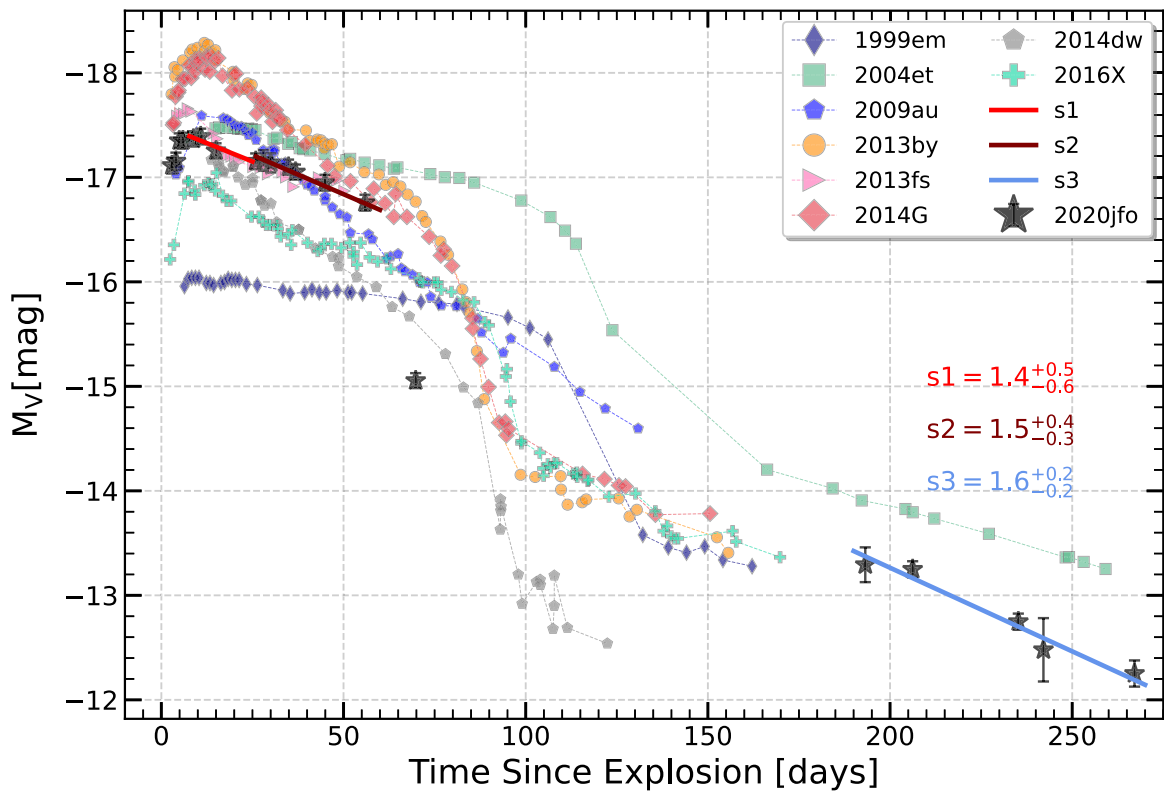


Figure 5. Absolute V-band light curve of SN 2020jfo is plotted with some other Type II SNe. Distance and extinction correction for individual objects are obtained from their references as provided in Section 3.3. The decline rates during early plateau (s1), late-plateau (s2), and the nebular (s3) phases determined using linear fit are also mentioned.

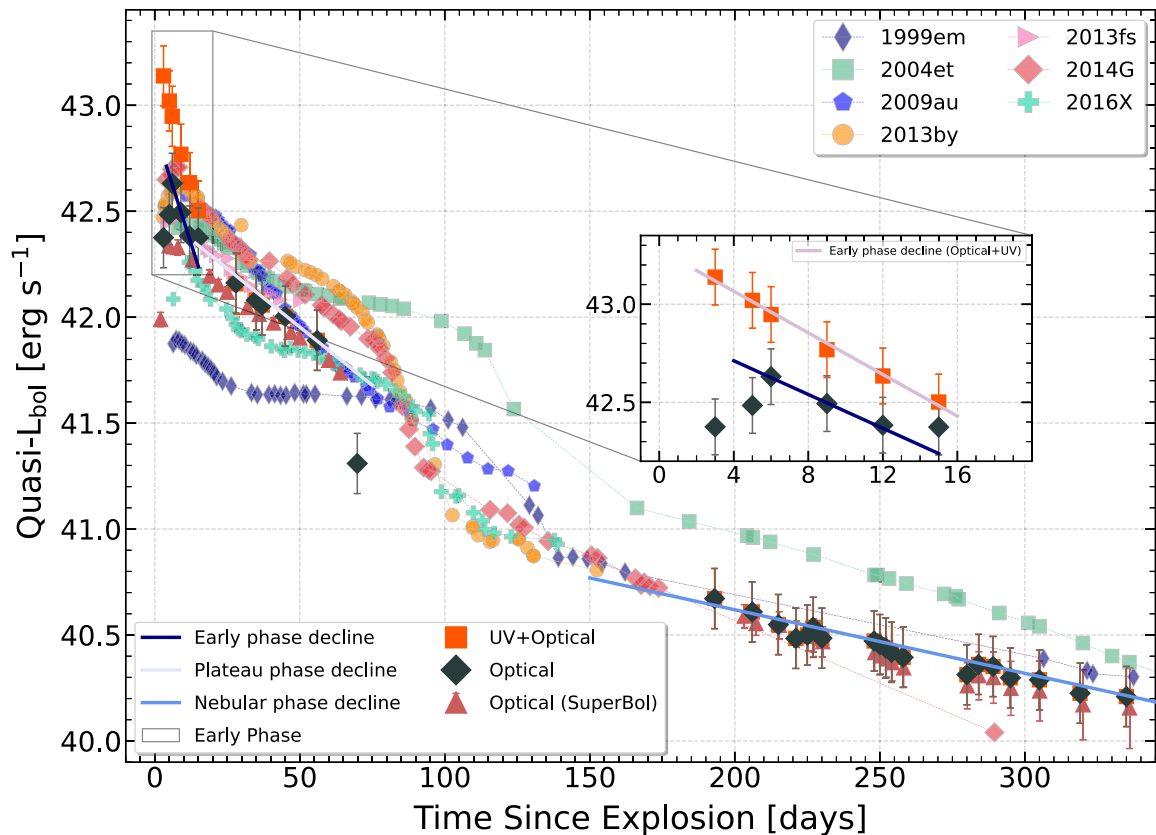


Figure 6. Quasi-bolometric light curve (Q-bol) of SN 2020jfo along with other Type II SNe. Q-bol with contribution from UV fluxes and from SuperBol (without BB-corrections) are also plotted. Inset shows Optical and UV+Optical Q-bol during early phase.

Table 6
Best-fit Slopes for Various Phases Where Decline Is Conspicuous in the Q-bol Light Curve of SN 2020jfo

SNe \Rightarrow	2020jfo	1999em	2004et	2009au	2013by	2013fs	2014G	2016X
Phases \Downarrow	Slopes (dex {log[L(erg s ⁻¹)] 100 day ⁻¹ })							
Early	$-4.00^{+1.02}_{-1.09}$	$-1.27^{+0.06}_{-0.05}$	$-1.33^{+0.02}_{-0.02}$	$-1.84^{+0.01}_{-0.01}$	$-1.60^{+0.01}_{-0.01}$	$-1.33^{+0.01}_{-0.01}$	$-1.32^{+0.02}_{-0.02}$	$-1.56^{+0.02}_{-0.02}$
Plateau	$-0.91^{+0.19}_{-0.20}$	$-0.08^{+0.01}_{-0.01}$	$-0.22^{+0.01}_{-0.01}$...	$-0.89^{+0.01}_{-0.01}$...	$-0.98^{+0.03}_{-0.04}$	$-0.52^{+0.01}_{-0.01}$
Nebular	$-0.32^{+0.03}_{-0.04}$	$-0.30^{+0.01}_{-0.01}$	$-0.44^{+0.01}_{-0.01}$...	$-0.45^{+0.05}_{-0.04}$...	$-0.68^{+0.04}_{-0.03}$	$-0.77^{+0.02}_{-0.02}$
Early UV+Optical	$-5.33^{+0.42}_{-0.41}$

Note. Slopes for other Type II SNe have also been estimated for comparison wherever possible.

bolometric flux is $\approx 20\%$ at +3 days, which increases to $\approx 80\%$ at $\sim +15$ d and almost in entirety at $\sim +28$ days.

Clearly, discrete decline trends are visible in the Q-bol light curve where the initial decline from +6 d to +15 d is significantly steeper than other SNe. Each decline phase is linearly fitted using Python's `emcee` routine. For comparison, the slopes for other objects during similar phases are computed and tabulated in Table 6.

Q-bol light curve of SN 2020jfo peaks at $\sim 4.3 \pm 1.4 \times 10^{42}$ erg s⁻¹ in optical bands around +6 d, whereas we missed the peak in the UV+Optical data. During the very early phase, Q-bol declines at a rate of $4.00^{+1.02}_{-1.09}$ dex 100 day⁻¹ and $5.33^{+0.42}_{-0.41}$ dex 100 day⁻¹ in Optical and UV+Optical, respectively, whereas for the other SNe this early phase decline is less steeper. For the Type IIP events SN 1999em and SN 2004et, and SN 2013fs, we estimated an early phase decline of 1.27 dex 100 day⁻¹, 1.33 dex 100 day⁻¹, and 1.33 dex 100 day⁻¹, respectively. For SN 2009au (1.84 dex 100 day⁻¹), SN 2013by (1.60 dex 100 day⁻¹) and SN 2016X (1.56 dex 100 day⁻¹), we find the decline to be steeper than normal Type II SNe, but significantly lower than SN 2020jfo (see Table 6). During the plateau phase and nebular phase, we find decline rates for SN 2020jfo to be $0.91^{+0.19}_{-0.20}$ dex 100 day⁻¹ and $0.32^{+0.03}_{-0.04}$ dex 100 day⁻¹, respectively. Plateau-phase decline is found to be similar to SN 2013by (0.89 dex 100 day⁻¹) and SN 2014G (0.98 dex 100 day⁻¹). In terms of magnitude, the slope in the nebular phase is found to be $0.80^{+0.08}_{-0.10}$ mag 100 day⁻¹.

3.5. ⁵⁶Ni Mass

In addition to ionizing and heating the outer envelope, the shock assists in the synthesis of heavy radioactive nuclei that decay and radiate (Arnett 1980). Out of all these, ⁵⁶Ni is the most significant contributor whose decay results in the daughter nuclei ⁵⁶Co with a half-life of ~ 6.1 days. These daughter nuclei then decay to ⁵⁶Fe with a half-life of ~ 77.3 days.

To calculate the synthesized mass of ⁵⁶Ni, we employed two independent methods. First, we used the following relations by Hamuy (2003):

$$\frac{M(^{56}\text{Ni})}{M_{\odot}} = \frac{L_t}{L_*} \exp \left[\frac{(t_t - t_{\text{exp}})/(1+z) - t_{1/2}(^{56}\text{Ni})}{t_{e\text{-folding}}(^{56}\text{Co})} \right] \quad (1)$$

where $L_* = 1.271 \times 10^{43}$ erg s⁻¹, $t_{1/2}(^{56}\text{Ni})$ is 6.1 days, and the e -folding time of ⁵⁶Co decay used is 111.26 days. Using the quasi-bolometric luminosity from ~ 192 days onward as tail luminosity, L_t , the mass of synthesized ⁵⁶Ni is estimated as $0.019 \pm 0.005 M_{\odot}$. It is to be noted that IR contribution to the

bolometric luminosity is not included, and hence, it could be considered as a lower limit on ⁵⁶Ni mass.

Second, we compared the late-phase quasi-bolometric luminosity of SN 2020jfo with that of SN 1987A. For SN 1987A, the bolometric luminosity and the mass of ⁵⁶Ni synthesized in the explosion are estimated with significant accuracy ($0.075 M_{\odot}$, Turatto et al. 1998). Assuming that the γ -ray deposition in SN 2020jfo is similar to SN 1987A, mass of ⁵⁶Ni in SN 2020jfo was estimated using, $M_{\text{Ni}} = M_{\text{Ni}}(1987A) \times L_{\text{bol}}(2020jfo)/L_{\text{bol}}(1987A)M_{\odot}$. If a constant fraction of about 35% (as estimated by Patat et al. 2001 and Elmhamdi et al. 2003b) is added to the quasi-bolometric flux to account for missing near-IR (NIR) flux, the mass of ⁵⁶Ni synthesized in SN 2020jfo becomes $0.033 \pm 0.004 M_{\odot}$, which is consistent with our earlier estimate if a similar IR correction is used. This value is also typical of Type II SNe as it is similar to the mean value of ⁵⁶Ni mass ($=0.033 M_{\odot}$) obtained by Anderson (2019) for a sample consisting of more than 40 Type II SNe.

It was empirically shown by Elmhamdi et al. (2003b) that the ⁵⁶Ni mass anticorrelates with the maximum of the steepness parameter ($S = dM_V/dt$) during the transition from the plateau phase to the nebular phase. This relation was further refined by Singh et al. (2018a) by incorporating a larger sample of Type IIP SNe including low-luminosity events. Mass of ⁵⁶Ni estimated using steepness parameters of 0.143 mag day⁻¹ (refer Section 3.2) is $0.030 \pm 0.002 M_{\odot}$, which is similar to earlier estimates.

Maguire et al. (2012) showed that the mass of ⁵⁶Ni is correlated with full width at half maximum of H α feature during the late-nebular phase. The FWHM of H α line was measured in the spectrum obtained at +292 days by fitting a Gaussian profile. The observed FWHM was corrected for instrumental broadening using the width of the night-sky emission lines present in the spectrum. Mass of ⁵⁶Ni estimated using this method is found to be $0.047^{+0.005}_{-0.004} M_{\odot}$, which is higher than our earlier estimates. It clearly signifies a broadened line emission profile in SN 2020jfo, implying a larger velocity dispersion in the line forming region, whereas in a typical Type IIP SN, the dispersion would have been lower due to a massive hydrogen envelope.

4. Spectroscopic Evolution

The optical spectral sequence of SN 2020jfo spanning from +3 days to around +292 days is shown in Figure 7. The spectral evolution at various phases together with a comparison to other Type II SNe is discussed in this section.

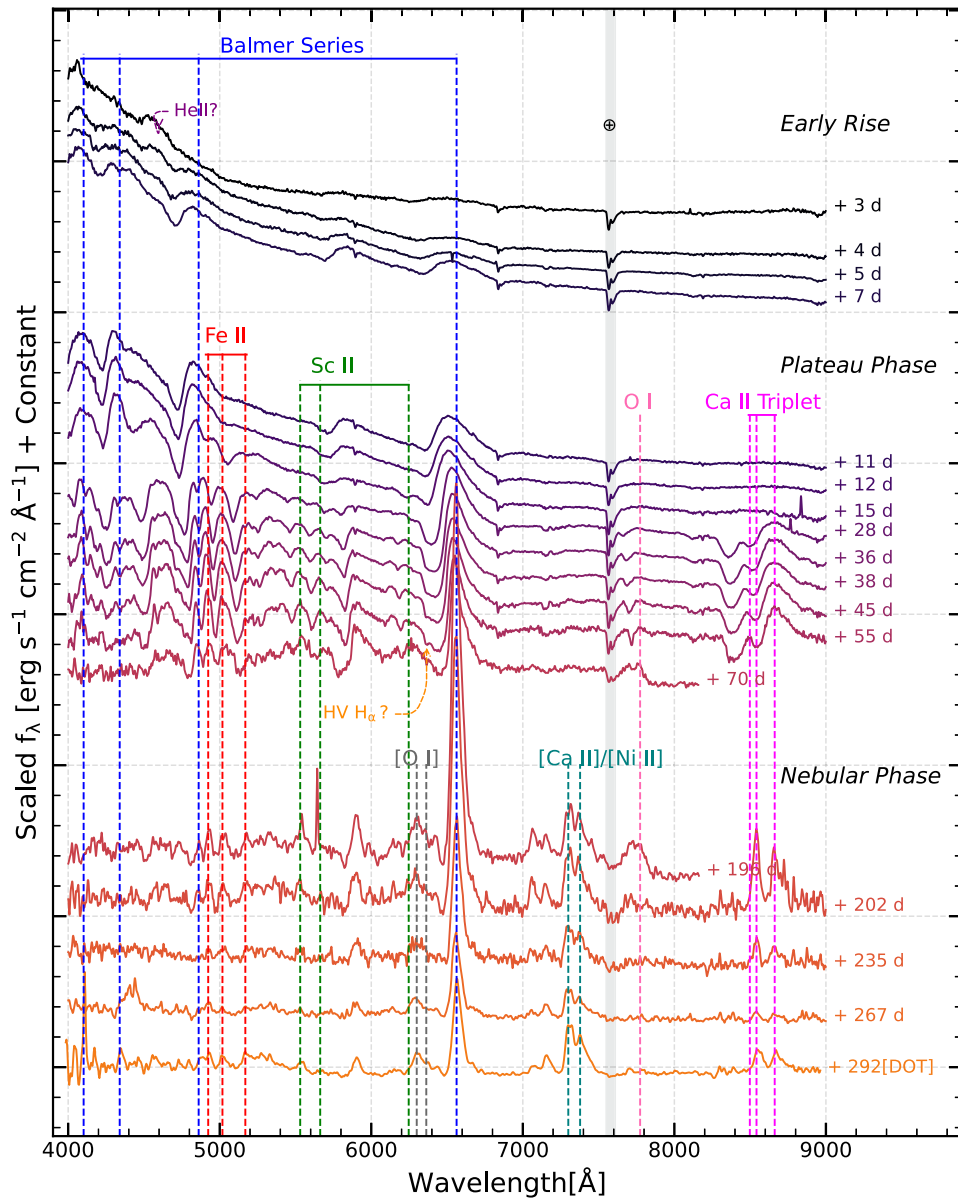


Figure 7. Spectral evolution of SN 2020jfo from 3 days until 292 days post explosion. Lines have been identified following Gutiérrez et al. (2017b), some of the prominent lines are marked. All spectra are flux calibrated and corrected for reddening and redshift.

(The data used to create this figure are available.)

4.1. Premaximum Spectral Evolution

In the first spectrum obtained on +3 days, we detect a broad-absorption trough at 6266 Å, which is likely due to H α and yields a line velocity of around 13,500 km s $^{-1}$ (see Figure 7, 8). If we look for a H β counterpart at a similar velocity, we should detect an absorption dip at 4650 Å. Instead, we observe a broad P-Cygni feature with emission at around 4686 Å and its absorption counterpart at roughly 4466 Å. The feature is likely a broad feature of He II 4686 Å at roughly 14,000 km s $^{-1}$, consistent with the line velocity of H α feature. This feature faded after +4 days, and a feature redward of this started appearing, which was identified as H β owing to a similar velocity with the H α feature. Broad He II 4686 Å was also seen in SN 2013fs (Bullivant et al. 2018; Chugai 2020) and is indicative of the presence of a cold dense shell (CDS) above the photosphere. The He II feature has a blue-skewed boxy

profile that suggests a geometrically thin and unfragmented CDS (Chugai 2020). The presence of He II in the early spectrum typically arises from the rapid recombination resulting from the interaction of the SN ejecta with extended supergiant atmosphere (Bruch et al. 2021); however, these would lead to the existence of narrow emission lines in the spectrum. The presence of a broad P-Cygni feature indicates that the line originated in the SN ejecta. This would require that the ejecta and the nearby CSM are highly ionized by the passage of the shock, which was also seen in SN 2006bp (Quimby et al. 2007).

To ascertain the identification of the He II feature in the early spectra, we used rapid spectral modeling code TARDIS (Kerzendorf & Sim 2014). Incorporating modifications from Vogl et al. 2019, TARDIS is now capable of synthesising spectra for Type II events as well. For our initial setup, we used

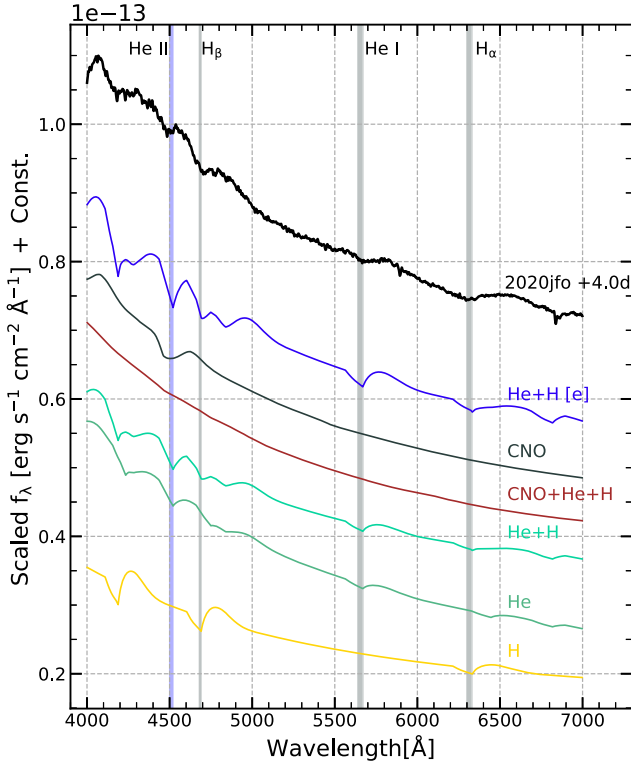


Figure 8. Early phase (+4.0 days) spectrum of the SN 2020jfo is compared with synthetic spectra generated using TARDIS, indicating the presence of ionized helium. The relative contributions due to different elemental compositions are plotted. In the square brackets, “e” implies the enhanced abundance for He in the composition.

a uniform density configuration with a density profile in the form of power law (Vogl et al. 2019). Hydrogen was treated in the nonlocal thermodynamic equilibrium approximation. We used different compositions for the outer layers, including CNO, H only, He only, H+He only, and H+He+CNO. We fixed luminosity parameters for +4 days calculations and used temperature as a free parameter. The observed velocities ($\sim 14,000$ – $16,000$ km s $^{-1}$) in the spectrum are used as velocities of the envelope layers. The resulting spectral luminosity was scaled with distance to obtain the observed-flux values. The synthesized spectra along with the SN 2020jfo spectrum at +4 days are shown in Figure 8. It was noticed that reproducing the ionized-helium feature required a temperature range of ~ 9000 to ~ 18000 K along with a higher helium abundance than solar values. On the other hand, for this feature to be a blend of nitrogen and carbon, the modeling required much-higher CNO abundances that are almost orders of magnitude higher than the solar values and is rather nonphysical. However, some amount of blending along with the helium could not be ruled out altogether. This strengthens the case that the observed broad-absorption feature is likely a He II feature.

The spectrum obtained during +4 days to +7 days shows gradual development of Balmer spectral features. Absorption trough around 5600 Å is seen in the spectrum obtained on +4 days that is likely due to He I 5876 Å, which evolved into a fully developed P-Cygni profile on +7 days. As the SN evolves, the continuum becomes redder. The spectrum of SN 2020jfo obtained on +3 days is compared with the spectrum of some other objects at comparable epochs and

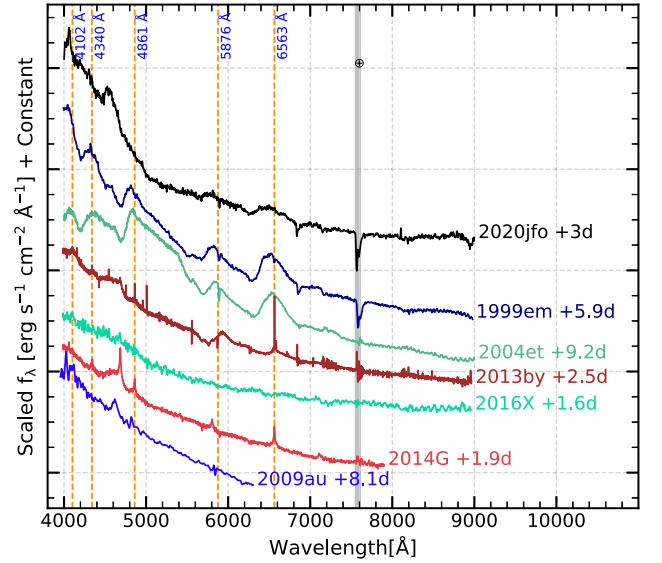


Figure 9. The premaximum (+2.8 days) spectrum of SN 2020jfo compared with the spectra of other Type II SNe at similar early phase.

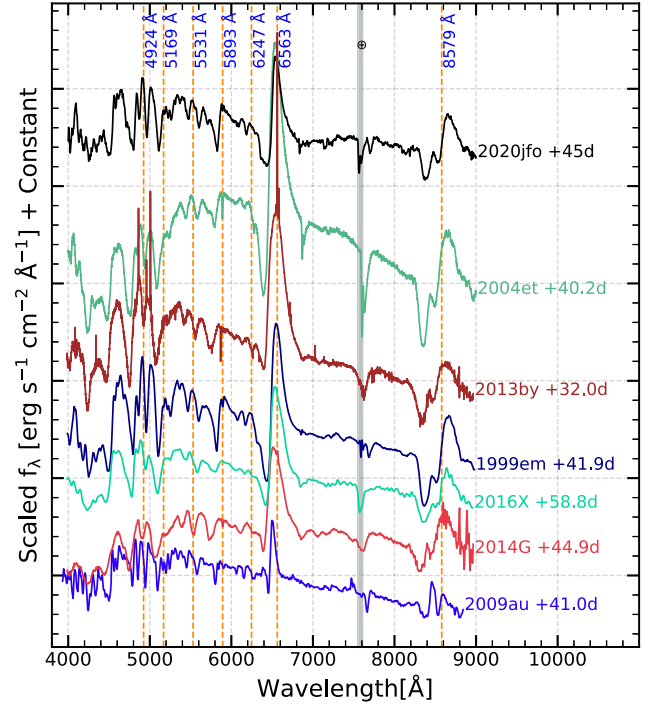


Figure 10. Spectrum of SN 2020jfo during the plateau phase (+44.9 days) compared with other Type II SNe at a similar epoch.

shown in Figure 9. The early phase spectrum of SN 1999em and SN 2004et shows a blue continuum with broad absorption due to hydrogen Balmer lines, while the early spectrum of SN 2009au, SN 2013by, and SN 2014G show narrow flash-ionized lines. The spectrum of SN 2020jfo appears different than the other objects with shallow absorption due to H α and the presence of broad absorption due to He II.

4.2. Plateau-phase Spectral Evolution

As the SN enters the plateau phase, the photosphere cools to the recombination temperature and stays in the hydrogen envelope leading to the development of various metallic lines

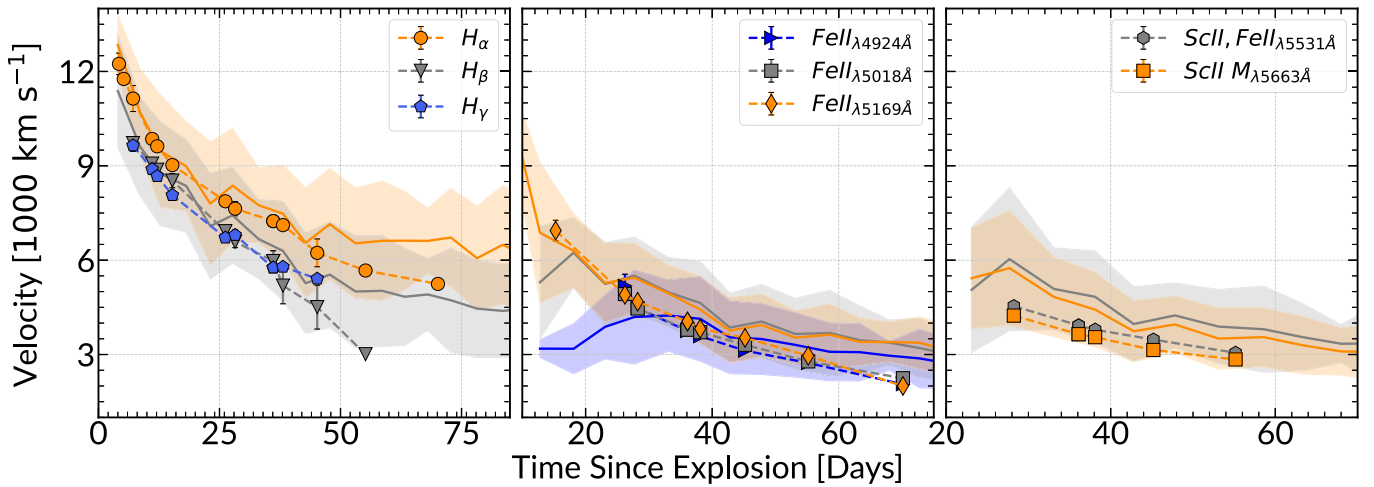


Figure 11. Line velocity evolution of Balmer, Fe II, and Sc II features obtained using their absorption minima are shown here. A comparison with mean Type II SNe velocities from Gutiérrez et al. (2014) is also shown. The solid line represents mean value while the shaded region displays the 1σ scatter from the mean.

of iron, scandium, oxygen, and calcium in the spectra. He I feature in the early phase slowly vanishes by +15 days, and the Na I D feature from the SN appears in its place. The shallow absorption feature seen at 5000 Å in the spectrum obtained on +12 days is due to the Fe II (multiplet 42) features at 4924, 5018, and 5169 Å. This feature strengthens as the photosphere moves deep inside the hydrogen envelope. Hydrogen Balmer lines become stronger, and other metallic lines such as Sc II (5663 Å), Sc II/Fe II (5531 Å), He I/Na I D, Ba I, and calcium NIR triplet develop in the spectra. We also detect O I 7774 Å absorption feature in the spectrum of +28 days.

The spectrum of SN 2020jfo obtained around +45 days is compared with the spectra of some other well-studied objects in Figure 10. Most spectral features are identical in all the Type II SNe used for comparison. The H α absorption feature in SN 2020jfo is shallower compared to the normal Type II SNe like SN 1999em and SN 2004et, whereas it is similar to fast-declining Type II SNe such as SN 2009au, SN 2013by, and SN 2014G. Further, in SN 2020jfo, the H α absorption trough is broader than other objects.

The velocities inferred from the metallic lines are similar, and they fall in the range $\sim 5000 \text{ km s}^{-1}$ at +28 days to $\sim 2000 \text{ km s}^{-1}$ at +70 days. The expansion velocities obtained using various species are compared with velocity estimates for a larger sample of Type II SNe (Gutiérrez et al. 2014) and are shown in Figure 11. Except for the early phase ($< +25$ days), where a steep decline in the H α velocity is observed, the velocities measured using H α , H β , and H γ lines are similar to the average velocity for Type II sample and closely follow the observed trend in Type II SNe throughout the photospheric phase. The velocities calculated using Fe and Sc lines are found to be marginally lower than the mean velocities of the Type II sample. This might indicate that SN 2020jfo was an explosion with lower energy; albeit the higher luminosity indicates otherwise. The steep decline observed during the early phase in the H α velocity could possibly hint toward the slowing down of outer layers while encountering circumstellar matter around the progenitor. Nevertheless, if we look at Figure 6, we could see that the higher luminosity, in comparison to other Type II events, is only visible initially and reaches a moderate value later achieved through a faster decline, again indicating a short-lived source of secondary radiation, likely CSM.

From +36 days onward, the H α absorption feature starts to broaden up, and a deep and narrow absorption feature (Cachito) starts to develop blue-wards of H α . This feature is prominently visible on the spectrum of +55 days at a wavelength of 6365 Å. The possibility of this feature arising due to Si II 6355 Å (Valenti et al. 2014) or Ba II 6497 Å was explored. The Cachito absorption lies redwards of the rest-wavelength of Si II and is hence unlikely to be related to it. Assuming the feature originated due to the Ba II line, the line velocity inferred is $\sim 6000 \text{ km s}^{-1}$, which is almost twice the velocity obtained from other metal lines ($\sim 3000 \text{ km s}^{-1}$ for Fe II) at the same epoch.

Chugai et al. (2007) proposed the emergence of high-velocity absorption features of hydrogen as a result of the interaction between the RSG wind and SN ejecta. We also explored the possibility of this feature being a high-velocity feature of hydrogen. The measured velocity of this HV-H α feature is $\sim 9000 \text{ km s}^{-1}$, and this velocity is similar to the postmaximum expansion velocity of H α . However, we did not observe a clear H β counterpart, likely due to the blending of several metallic lines in that region. This HV feature is similar to the “narrow and deeper” Cachito, seen in (Gutiérrez et al. 2017b, e.g., SN 2003hl) a Type II SN sample study, and is similar to the case of low-velocity/low-luminosity SNe, where no H β counterpart is seen. The likely presence of the HV feature of H α in the photospheric spectra favors the case of circumstellar interaction (Gutiérrez et al. 2017b).

4.3. Nebular-phase Spectral Evolution

Nebular spectra of SN 2020jfo during +196 days to +292 days are plotted at the lower panel of Figure 7. As the recombination phase ends, the photosphere recedes into the innermost part of the ejecta. The luminosity during this phase varies in direct proportion to the ^{56}Ni , which was synthesized during the explosion (Srinivasaragavan et al. 2021). The light curve in this phase is mainly powered by the radioactive decay of ^{56}Co to ^{56}Fe . The nebular-phase spectrum of SN 2020jfo is dominated by prominent emission lines of Na I D, [O I], H α , and [Ca II].

Narrow emission lines from metals are also seen, which become progressively more prominent as the SN evolves into the late-nebular phase. The bluer part of the spectrum is

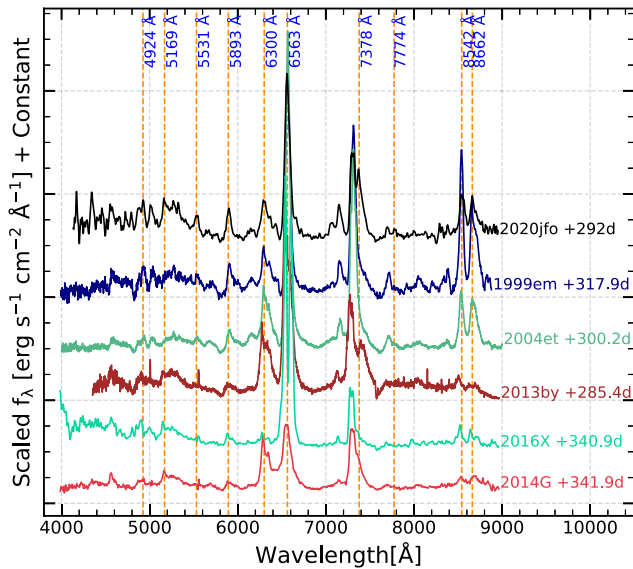


Figure 12. Spectrum of SN 2020jfo during the nebular phase (+292.2 days) is compared with other Type II SNe at similar epochs.

dominated by lines due to Fe, Ba, Sc, Mg, etc. Hydrogen Balmer lines are seen with decreased absorption strength. As the medium becomes more rarefied, forbidden lines of Fe, Ca, and O appear in the spectrum. The prominent lines seen in the nebular-phase spectrum are identified and marked in Figure 13. The spectra taken during this phase could be used to estimate the zero-age-main-sequence (ZAMS) mass of the progenitor when compared with line strengths of model spectra at similar phases. This method has been deployed in many cases in the literature to constrain the progenitor mass of Type II SNe (e.g., Szalai et al. 2019; Van Dyk et al. 2019; Hiramatsu et al. 2021b).

The nebular spectrum of SN 2020jfo at +292 days is compared with nebular-phase spectra of other Type II SNe at similar epochs (see Figure 12). We find that the prominent emission lines of [O I], H α , [Ca II], and Ca II NIR triplet is similar to that of other normal and fast-declining Type II SNe. However, if we look closely, the spectrum of SN 2020jfo shows a clear blue excess and a forest of features due to lines of [Fe II] and Fe II (Figure 13). The Na I D feature in SN 2020jfo is similar to that of normal Type II SN 1999em but is more pronounced in comparison to fast-declining events SN 2013by and SN 2014G. The red-wing of [Ca II] shows a clear secondary peak due to [Ni II], which is not seen in normal Type II SNe like SN 1999em and SN 2004et, but seen in the fast-declining Type II SN 2013by.

5. Characteristics of the Possible Progenitor

In this section, we perform the observational analysis along with the semi-analytical and hydrodynamical modeling to discuss possible progenitor scenarios for SN 2020jfo.

5.1. Semi-analytical Modeling

To obtain estimates on progenitor properties, we used a semi-analytical model described in Nagy & Vinkó 2016, which was initially described by Arnett & Fu (1989). It models the SN as a two-component system consisting of a core region that is dense and a shell region with a low-mass extended envelope. It

assumes that the SN ejecta is spherically symmetric and expanding homologously. For the density profile of the ejecta, the core region is assumed with a flat or constant density profile with a constant Thompson-scattering opacity of $\kappa = 0.4 \text{ cm}^2 \text{ g}^{-1}$ whereas the shell region has a density profile that decreases as a power-law function ($n=2$) or as an exponential ($a=0$) with an opacity of $\kappa = 0.2 \text{ cm}^2 \text{ g}^{-1}$ (Nagy & Vinkó 2016). We obtained an ejecta mass of $\sim 7.5 M_{\odot}$ (core + shell), a RSG radius ranging from 310–340 R_{\odot} , and a total energy (thermal and kinetic) of ~ 3 foe based on the best-fitting model shown in Figure 14. The mass of ^{56}Ni obtained from this semi-analytical model, with the amount of gamma-leakage added to the model to follow the nebular light-curve evolution is $0.03 \pm 0.01 M_{\odot}$, which is in corroboration with our earlier estimates.

5.2. Estimate from Nebular Spectrum

To constrain the progenitor mass, we compared the nebular-phase spectrum of +292 days with model spectra from Jerkstrand et al. (2014; Figure 15). The model spectra for different progenitor masses, viz. 12, 15, 19, and 25 M_{\odot} , have been scaled with respect to ^{56}Ni mass and the distance of SN 2020jfo (in contrast to 5.5 Mpc for model spectra). In order to account for the difference in phase between the model spectra and the observed spectrum, the observed spectrum was scaled by the amount determined from the characteristic timescale of ^{56}Ni -decay chain and the dissimilarity in phases. The comparison of [O I] 6300, 6364 Å line fluxes of the observed spectra with the spectral models suggest a lower-mass progenitor of $\sim 12 M_{\odot}$. However, the flux of H α is quite weak compared to the 12 M_{\odot} progenitor, indicating a stripped hydrogen envelope in SN 2020jfo. In a CCSN, the mass of calcium synthesized is insensitive to the ZAMS mass of the progenitor, whereas the mass of oxygen synthesized depends on it, and the [Ca II] / [O I] flux ratio is an indicator of the progenitor mass (Fransson & Chevalier 1989). The observed [Ca II] / [O I] flux ratio of ~ 1.5 in the spectrum of ~ 292 days is also suggestive of a low-mass progenitor for SN 2020jfo.

SN 2020jfo is also one of the few hydrogen-rich SNe where a clear, distinct spectral feature of [Ni II] 7378 Å is seen adjacent to the [Ca II] feature in nebular-phase spectral evolution. The feature has its origins from stable ^{58}Ni , synthesized during explosive nucleosynthesis (Jerkstrand et al. 2015a). Following the methodology described in Jerkstrand et al. 2015b, we computed a Ni/Fe luminosity ratio for SN 2020jfo (see Figure 16) as 2.10 ± 0.43 (similar to the value obtained in Sollerman et al. 2021). This translates to a Ni/Fe ratio by mass as 0.18 ± 0.04 , which is roughly 3.0 ± 0.6 times the solar value. This could be achieved either by a neutron excess usually found in the Silicon layer or due to a very high progenitor metallicity ($>5 Z_{\odot}$) that increases the neutron excess in oxygen shell (Jerkstrand et al. 2015a). The estimated metallicity close to the SN site is $\sim 1.5 Z_{\odot}$, which is not high enough to produce such a Ni/Fe ratio in the ejecta. The only plausible scenario for such excess is seen in spherically symmetric models of $M_{\text{ZAMS}} \lesssim 13 M_{\odot}$ (Jerkstrand et al. 2015a) that house a thick Si layer with a neutron excess. This is concurrent with our estimates of a lower-mass progenitor.

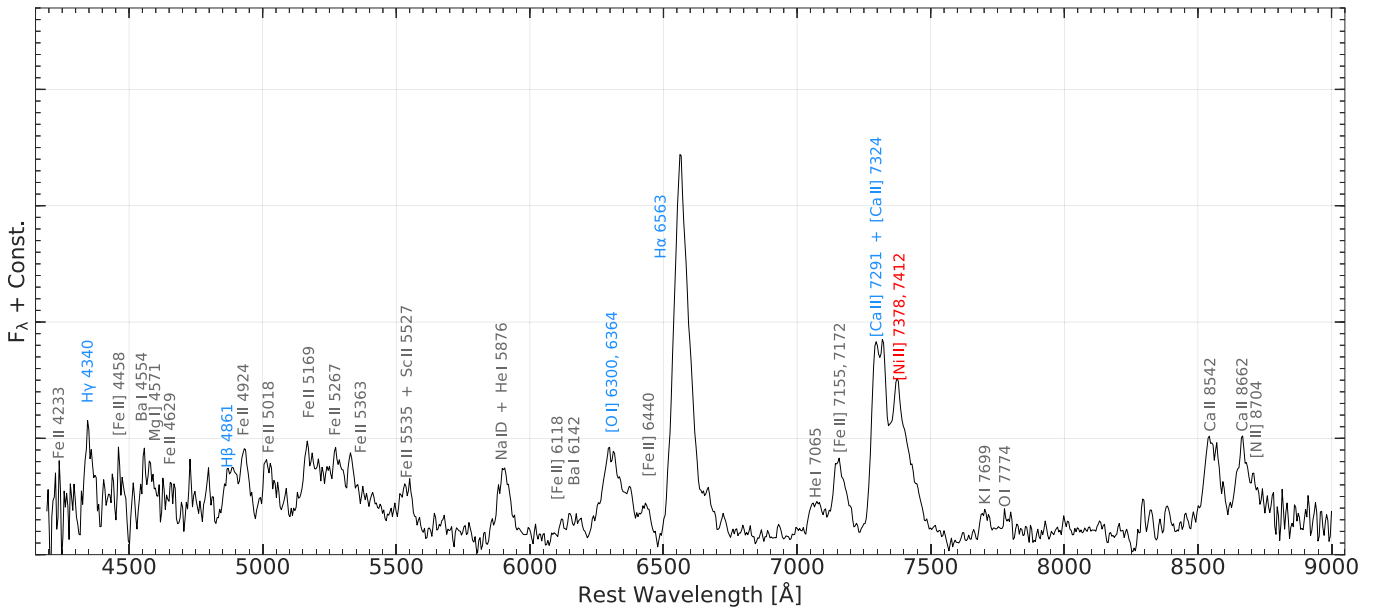


Figure 13. Identification of lines in the nebular spectrum (+292 days) of SN 2020jfo.

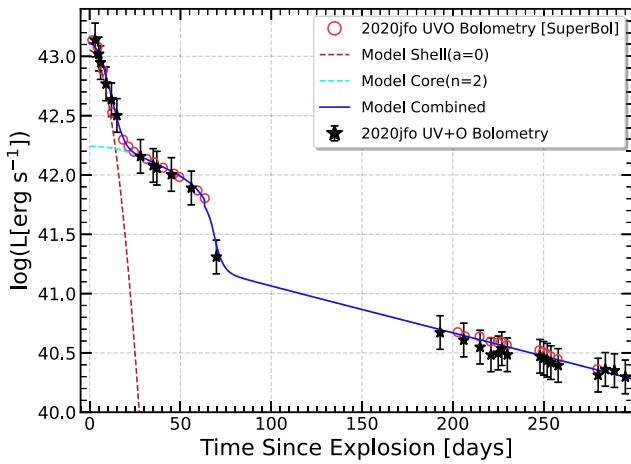


Figure 14. Best-fitting model curves to the bolometric light curve using two-component model from Nagy & Vink (2016). Individual contributions from the shell and core component are shown with the combined bolometric luminosity.

5.3. Hydrodynamical Modeling

We resort to detailed hydrodynamical modeling for better constraints about the progenitor, its evolution, mass-loss history, and its immediate environment. We used the publicly available 1D stellar evolution code MESA $r-15140$ (Paxton et al. 2011, 2013, 2015, 2018, 2019) and a simplified version of STELLA (Blinnikov & Sorokina 2004; Baklanov et al. 2005; Blinnikov et al. 2006) included with MESA to simulate light curves and photospheric velocities of SN 2020jfo. MESA + STELLA has been successfully used in many studies to investigate properties of Type IIP SNe progenitors (Moriya et al. 2011; Goldberg et al. 2019; Hiramatsu et al. 2021a). We also try this framework to get more insights about the progenitor of SN 2020jfo. Some of the aspects regarding various hydrodynamical parameters are as follows:

1. The built-in nuclear reaction rates were taken from “approx21_cr60_plus_co56.net.” Nuclear reaction rates are

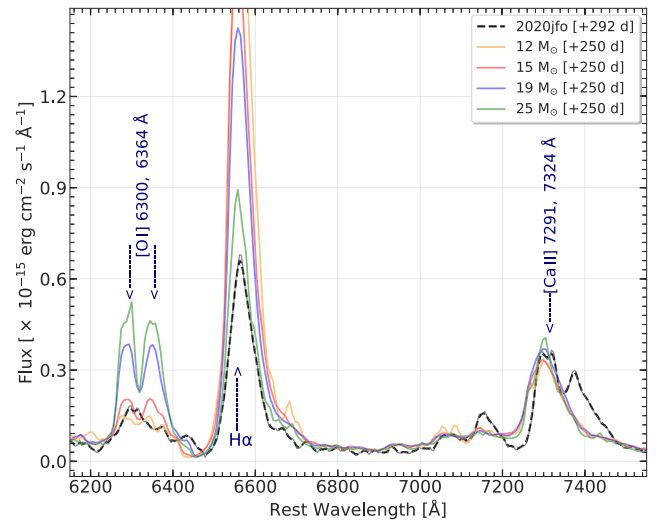


Figure 15. Nebular spectrum (+292 days) of SN 2020jfo is compared with the model spectra for 12, 15, 19, and 25 M_{\odot} models, at 250 days since explosion. The model spectra obtained from Jerkstrand et al. (2014) are scaled for distance and nickel mass, and corrected for phase mismatch using the characteristic decay time corresponding to SN 2020jfo.

mostly from the Nuclear Astrophysics Compilation of Reaction rates, (Angulo 1999) and the Joint Institute for Nuclear Astrophysics, JINA reaction rates (Cyburt et al. 2010).

2. Cool and hot wind schemes for the red giant branch or asymptotic giant branch phase are taken as “Dutch.” as described in MESA IV. This wind scheme for massive stars is a combination of results from work by various Dutch authors. The particular combination chosen is based on the work by Glebbeek et al. (2009). Typically, if the surface hydrogen has a mass fraction less than 0.4 and an effective temperature greater than 10^4 K, the prescription used is from Vink et al. (2001); otherwise it is taken from Nugis & Lamers (2000).

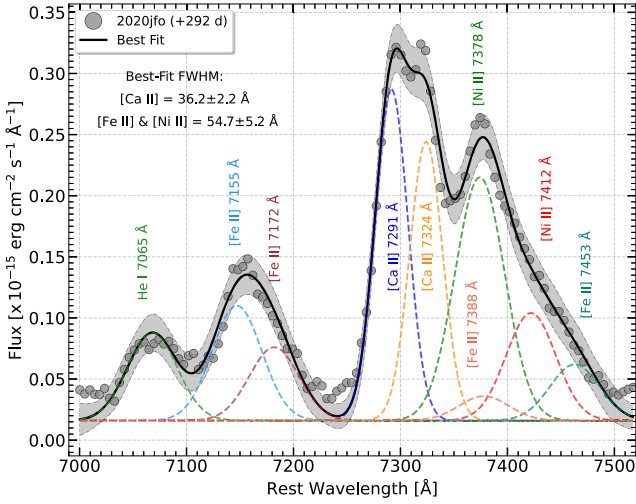


Figure 16. Multicomponent Gaussian fit to the nebular spectrum of SN 2020jfo (+292 days). The fit was performed by having different values of line broadening for [Ca II] and [Fe II]/[Ni II] owing to their differing origins in the ejecta. The FWHM values obtained are mentioned in the figure.

3. The mixing length parameter (MLT_option) is set to *Heney*, which is based on the work by Heney et al. (1965), with $\alpha_{MLT} = 1.5$, where α_{MLT} is the ratio of mixing length to the pressure scale height ($= P/g\rho$).
4. To determine the position of the convective boundaries, the default *Ledoux* criterion is used.

From the evolution of premain-sequence star to finally retrieving the optical light curve post-explosion, the modeling process was completed in three steps inside the MESA framework. First, a pre-MS star was evolved until the Fe-core developed, and there was an onset of rapid infall of the iron core. It was accomplished using “make_pre_ccsnIIP” test suite provided in MESA. Default values of the controls in `inlists` were used with slight variations for convergence with help from Farmer et al. (2016). We fixed our metallicity to $Z = 0.024$ as estimated in Section 3.1 for all the simulations.

Since the explosion could not be achieved directly by MESA, we proceeded to the second step, which closely followed the “ccsn_IIP” test suite. In this step, a section of the core was removed, which would have eventually collapsed onto a proto-NS. This center section was removed from the model at the location where entropy/baryon $= 4k_B$. Later, the explosion was induced by the synthetic injection of energy into a thin layer of $\approx 0.01 M_{\odot}$ at the inner boundary for 5 ms, and the rate was scaled such that the E_{exp} reached the desired input value. Shock then proceeded through the various steps until it reached just below the surface where the hand-off was performed from MESA to STELLA (Paxton et al. 2018). STELLA then dealt with the shock-breakout and post-explosion evolution. For the second step, we did not vary the ^{56}Ni mass estimate of $0.033 M_{\odot}$ obtained in Section 3.5 in order to reduce the parameter space.

A recent study by Hiramatsu et al. (2021a) discusses the possibility of obtaining shorter plateaus in Type II SN light curves from progenitors with ZAMS mass of $18\text{--}25 M_{\odot}$ with an enhanced mass loss ($\dot{M} \approx 10^{-2} M_{\odot} \text{ yr}^{-1}$) in the decades prior to collapse. The objects of interest in their study were more luminous events (Peak $M_V < -18 \text{ mag}$), with a higher ^{56}Ni yield and higher expansion velocities in contrast to SN 2020jfo, which has an average ^{56}Ni mass and

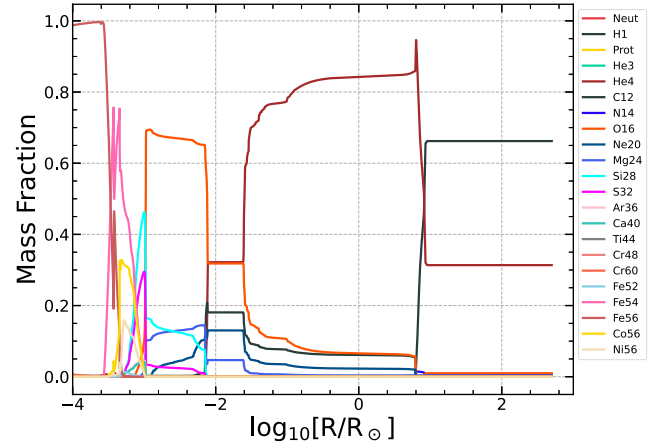


Figure 17. Presupernova mass fractions for an evolved $12 M_{\odot}$ model for different species present in the “approx21_cr60_plus_co56.net” (approx21) network used in MESA modeling.

lower-expansion velocities in comparison to a typical Type II SNe. In addition, a number of other numerical modeling works (Dessart et al. 2010; Sukhbold et al. 2016) showed that low-mass progenitors of $M \leq 18 M_{\odot}$ were not able to produce a shorter plateau duration of around 60 days. In all, none of the simulations for masses $M \leq 15 M_{\odot}$ under standard conditions were able to produce light curves with short plateaus (Dessart et al. 2010; Sukhbold et al. 2016; Curtis et al. 2020; Hiramatsu et al. 2021a). Instead of exploring the parameter space favored by other works for short-plateau Type II SNe, we took a different approach, where the inputs were driven from the results of semi-analytical modeling and nebular-phase spectra. Hence, we went ahead with the evolution of a ZAMS model of $12 M_{\odot}$ and tried variations in the evolution schemes to achieve a shorter plateau.

A $12 M_{\odot}$ progenitor was evolved with an initial metallicity slightly higher than solar and with a finite amount of rotation ($\Omega = 0.1 \Omega_{\text{critical}}$). Figure 17 shows the pre-SN mass fractions of an evolved model for “approx21” network. It was found that, for a typical mass-loss rate due to winds, a short plateau was not possible as there was not enough stripping of the hydrogen envelope of the progenitor’s ejecta. Hence, an enhanced mass loss due to winds was applied during the evolution, which is highly possible in a higher-metallicity environment with a rotating progenitor. Mass loss was controlled by the wind scaling factor (wsf) in MESA. We tried varying this parameter from a default value of 1.0 onwards. At a value of $wsf = 5.0$, we could get enough material stripped off from its surface in order to achieve a short plateau with a similar period as SN 2020jfo. We also note that the sharp transition could not be produced using physical mass-loss schemes. However, a sharp transition is achieved if the mass is removed by hand to leave the final mass as $5.0 M_{\odot}$. Exploring the amount of nickel mixing in layers, the density structure of the progenitor, etc. is beyond the scope of this work. Some of the models did not converge as the central density was not sufficient enough for the ignition of higher masses during the course of evolution. The simulated light curves obtained for various wsf along with Q-bol for SN 2020jfo are shown in Figure 18, and the corresponding pre-SN values for various models are presented in Table 7.

It was demonstrated by comprehensive modeling that the model with ZAMS mass $12 M_{\odot}$, and the final mass of the progenitor being $6.6 M_{\odot}$, fitted closely to the decline to

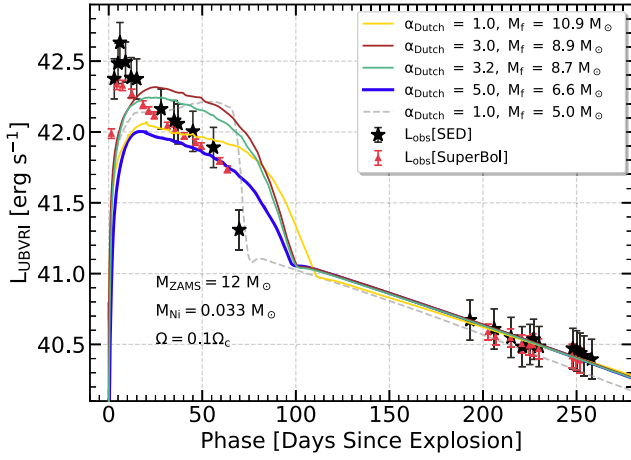


Figure 18. Quasi-bolometric light curves obtained from MESA + STELLA modeling with different values of wsf (1.0, 3.0, 3.2, and 5.0) for the $12 M_{\odot}$ ZAMS model. Q-bol of SN 2020jfo is overplotted for comparison.

Table 7
Pre-SN Parameters for Different Models

$M_i = 12.0 M_{\odot}, \Omega = 0.1\Omega_c, Z = 0.024$				
M_f (M_{\odot})	Age (Myr)	α_{Dutch}	Radius (R_{\odot})	E_{tot} (foe)
10.9	18.7	1.0	470	-0.94
8.9	19.2	3.0	780	-1.00
8.7	19.3	3.2	723	-0.93
6.6	19.7	5.0	679	-0.91

Note. Best-fitting model parameters are shown in bold.

nebular-phase and late-phase evolution of the observed light curve (Figure 18). It had an ejected mass of about $5 M_{\odot}$ and an excised core of about $1.6 M_{\odot}$. The explosion energy for best-fitting models was $E_{\text{exp}} = 0.2\text{--}0.4$ foe. The photospheric velocity evolution for this model is in agreement with the estimates from the observed spectral sequence (see Figure 19). Slow velocity evolution could also be attributed to the low energy of the explosion as obtained from hydrodynamic modeling (0.2–0.4 foe) along with the low ejecta mass as most of the mass was blown away by winds during evolution. A nickel mass of $0.033 M_{\odot}$ used in models substantiates our earlier Ni mass estimates. While the modeled light curve matched with the observed plateau duration, decline to the nebular-phase, and late-phase light-curve evolution, it failed to reproduce the early steep rise to a high luminosity observed in the quasi-bolometric light curve. As the calculations are based on normal Type IIP SNe, only primary radiation sources, viz. shock-breakout and cooling, hydrogen recombination, and radioactive decay, are considered. The inadequacy of the current model to fit the early part of the light curve indicates the need to introduce a secondary source of radiation for early times, and the best possible source could be the presence of CSM close to the progenitor.

Due to the lack of direct signatures of CSM interaction, we could not calculate the extent and density of the CSM. In order to estimate the same, we used STELLA, where it was possible to place the CSM around the progenitor with its configuration defined by the parameters wind velocity, mass-loss rate, and its duration. The density profile in STELLA is dependent on the

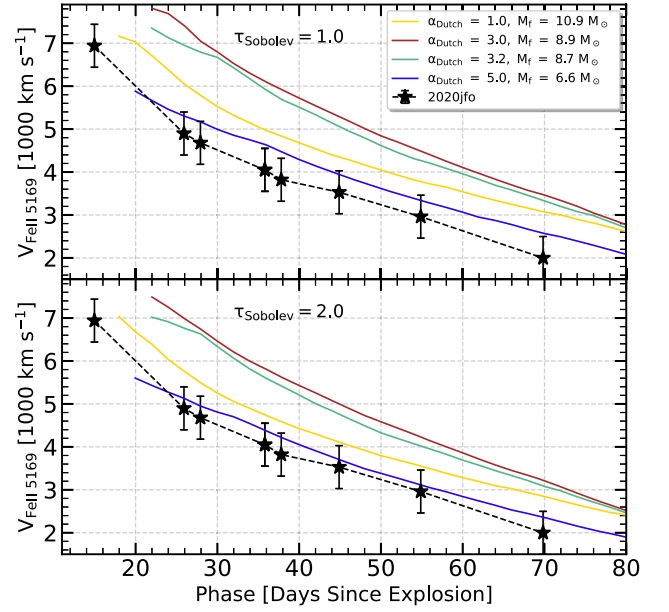


Figure 19. Photospheric velocity evolution as obtained from MESA + STELLA modeling for two different values of optical depth ($\tau_{\text{Sobolev}} = 1.0$ and 2.0) compared with the observed photospheric velocities.

radius, r , away from the progenitor’s center as follows:

$$\rho(r)_w = \frac{\dot{M}_w}{4\pi r^2 v_w}, \quad (2)$$

where \dot{M}_w is mass-loss rate in $M_{\odot} \text{ yr}^{-1}$ due to winds, and v_w is the wind velocity. We allocated 40 zones out of 400 for CSM configuration, and the bolometric flux was obtained at four extents (2, 10, 20, 40 au) with various mass-loss rates (0.001, 0.005, 0.01, $0.05 M_{\odot} \text{ yr}^{-1}$). A typical wind velocity of 10^6 cm s^{-1} was affixed for all configurations. The modeled light curve with $\dot{M} = 0.01 M_{\odot} \text{ yr}^{-1}$, $t = 20 \text{ yr}$ (which corresponds to a CSM extent of roughly 40 au) is found to fit the observed quasi-bolometric light curve well (see Figure 20). The He II feature considered as the proxy for the interaction signature is not observed beyond +10 days. This could be due to formation and increasing strength of other lines in the spectra. Furthermore, it could also be due to a decrease in CSM-ejecta interaction, giving rise to a steep decline in the quasi-bolometric light curve. Light-curve modeling is suggestive of interaction up to +15 days, which is considered as an upper bound. Further, we compare $U - B$ color evolution (Figure 21) of models with observed $U - B$ color. We find the color to be flat for the initial 8 days, and later it evolves toward red. This initial trend is only seen in the models with added CSM.

5.4. CSM Interaction

There have been numerous instances where studies have provided enough evidence for CSM surrounding Type II progenitors both in spectra and light curves. Förster et al. (2018) attributed the steeper light-curve rise and delayed shock emergence to the dense CSM from their sample of 26 Type II SNe. Another study, combining light-curve modeling and observations (Morozova et al. 2018), summarized that $\sim 70\%$ SNe have CSM, and the estimated CSM masses ranged

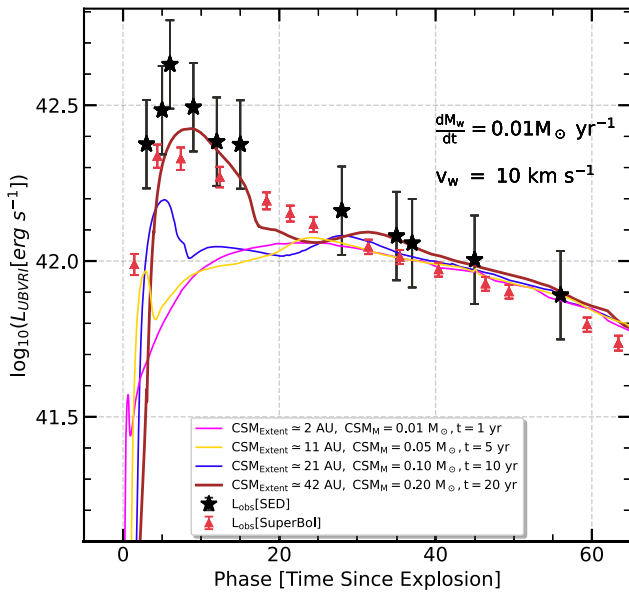


Figure 20. Quasi-bolometric light curves as obtained from MESA + STELLA modeling for a $12 M_{\odot}$ ZAMS progenitor ($M_f = 6.6 M_{\odot}$) with different CSM configurations. Q-bol light curve of SN 2020jfo is overlotted for comparison.

between 0.18 and $0.83 M_{\odot}$. Bruch et al. (2021) emphasized the appearance of narrow flash emission features, especially He II 4686 \AA , in the very early spectra, ideally taken within less than 48 hrs of the explosion. We do not see such narrow signatures of CSM interaction in our earlier spectra, although we do see broad-ionized lines of helium, which were likely formed at the CDS arising due to the shock ionization of the outer layers or the CSM close to the ejecta. Along with this, the presence of HV H α feature in the mid-to-late-plateau-phase spectra is an indication of CSM’s presence.

The higher peak luminosity and steeper early phase decline seen in SN 2020jfo also strengthen the case of CSM close to its progenitor. High decline rates in the early phase of Type II SNe have been attributed to the interaction with CSM. The diagnostic in SN 2013by was the presence of asymmetric line profiles with photospheric signatures of high-velocity features of hydrogen (Valenti et al. 2015). In SN 2014G, the presence of highly ionized spectroscopic features was attributed to a metal-rich CSM accumulated from the mass-loss events prior to the explosion (Terreran et al. 2016). It is likely that the higher luminosity of SN 2020jfo during the early epoch is due to interaction with the nearby CSM, and its density profile is such that this is not sustained for prolonged periods. We ascertained this possibility with hydrodynamical modeling using MESA + STELLA.

Furthermore, the color evolution of SN 2020jfo in the early phase is bluer as compared to other SNe, while in the late phase, it flattens out and merges with the normal Type II SN color evolution. The bluer early phase color evolution is similar to the CSM-interacting events. The Q-bol of SN 2020jfo during the early phase is comparable to SN 2009au and SN 2014G (see Figure 6), which showed clear signs of interaction in their spectra. Though the luminosity is higher during the early phase, the steeper decline in the plateau phase leads to a luminosity comparable to normal Type IIP events such as SN 2016X toward the end of the plateau. The additional source giving rise to the higher luminosity in the early phase is likely due to CSM interaction; however, the CSM remains hidden.

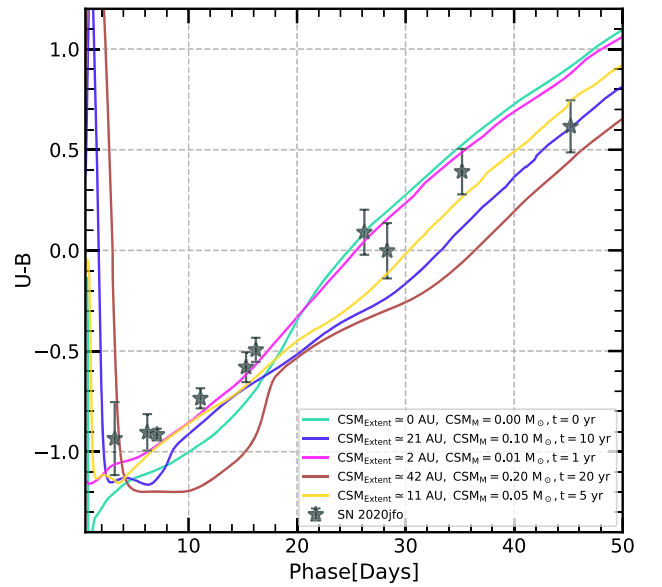


Figure 21. Color evolution as obtained from MESA + STELLA modeling for a $12 M_{\odot}$ ZAMS progenitor ($M_f = 6.6 M_{\odot}$) with different CSM configurations.

Nagao et al. (2020) showed that a CSM distributed in the form of a disk, when viewed from a polar angle, would only cause enhancement in flux due to heating effects and would not leave any signatures of interaction in the spectra. Although, as clearly shown in Nagao et al. (2020), overluminous Type IIP SNe might not be powered by such disk interaction, but a slight enhancement is a likely proposition during the early phase.

To have a complete picture, we also looked at the field of SN 2020jfo for any radio detection. The field was observed on 2021 October 17 (JD 2,459,504.5) in the VLA sky survey (VLASS; image cutouts can be found here¹⁰). No significant radio emission was detected at the SN position, and a flux density limit of $309 \mu\text{Jy}$ (3σ upper limit) at 3 GHz was obtained. Unsurprisingly, the SN being >500 days old at the time of VLASS observations, the radio flux density declined below the sensitivity limits of current radio telescopes around this period, even for radio-bright Type IIP SNe. Using the expression for mass-loss rate given in Weiler et al. 1986, we obtained an upper limit of $\dot{M} < 2.5 \times 10^{-5} M_{\odot} \text{ yr}^{-1}$. This value is somewhat consistent with typical Type IIP SNe but smaller for our case where we estimated a higher mass-loss rate (see Section 5.3) from the MESA+STELLA modeling of the early phase bolometric light curve. This is likely due to the difference in the epochs of observations of the radio and the modeled light curve with CSM. Sollerman et al. (2021) also looked for an X-ray emission post-explosion for SN 2020jfo and could only cite an upper limit based on their estimates. It might be the case that the X-ray emission from dense CSM was earlier on and could have been missed as it was absorbed by nearby CSM (similar scenario as pointed out in Jacobson-Galán et al. 2022).

5.5. Case for a Stripped Low-mass Progenitor

The metallicity estimated was slightly higher than the solar values and might have helped in escalating the mass-loss rate of the progenitor star. It has been argued in Dessart et al. 2013 that lower-envelope mass at higher metallicity ought to produce a

¹⁰ <http://cutouts.cirada.ca/>

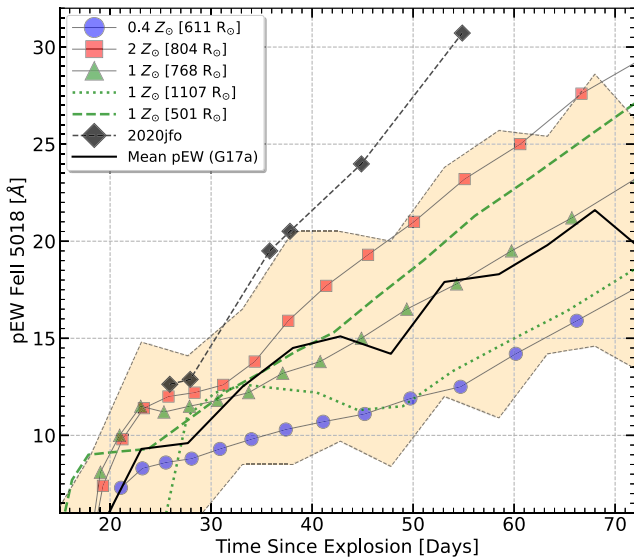


Figure 22. Temporal evolution of pEW of Fe II 5018 Å in comparison with models from Dessart et al. (2013) having different metallicities (0.4, 1, and 2 Z_{\odot}). The black solid line represents the mean value of the pEW of Fe II 5018 Å, and shaded region shows its dispersion from the extensive sample of Gutiérrez et al. (2017a).

Type II SN with a shorter duration plateau. A direct result of this is seen in the temporal evolution of pseudo-equivalent widths (pEW) of Fe II 5018 Å of SN 2020jfo in comparison to the estimates from spectral models from Dessart et al. (2013; see Figure 22). We find that, with increasing metallicities, the pEW increases. The higher pEW evolution of SN 2020jfo during the photospheric phase corroborates with the enhanced metallicity environment. However, the implied metallicity is much higher than that estimated for its host (i.e., $\sim 1.5 Z_{\odot}$ in Section 3.1). Dessart et al. (2013) have shown that the compactness (i.e., radius) of the progenitor affects the pEW of the metal features during the plateau phase. This is depicted in Figure 22, which shows 3 variants of $1 Z_{\odot}$ metallicity progenitor, with different final progenitor radii. Observationally, this indicates the presence of a stripped hydrogen envelope, which would make the progenitor more compact, and probably explain the lack of a clear early decline ($s1$) phase prior to the onset of the plateau ($s2$) phase.

The semi-analytical modeling of the bolometric light curve of SN 2020jfo in Section 5.1 infers a progenitor of low mass with an ejected mass, M_{ej} of $\sim 7.3 M_{\odot}$, and a RSG radius of $\sim 350 R_{\odot}$. Considering a typical NS remnant core of $\sim 1.5 M_{\odot}$, we infer a pre-SN mass of $\sim 9 M_{\odot}$.

From MESA+STELLA modeling, we obtained a stripped progenitor with a pre-SN mass of $\sim 6.6 M_{\odot}$ where the initial ZAMS mass was $12 M_{\odot}$. A similar ZAMS value for the progenitor was also obtained using late-nebular spectra (see Section 5.2). However, we did not implement any synthetic mass-loss scheme (deliberate removal of the H envelope mass) to achieve stripping of the progenitor (see Section 5.3). Nevertheless, there could be numerous short time windows where enhanced mass loss is possible (Decin et al. 2006), which are hard to predict and hence challenging to include in modeling. Observationally, mass-loss rates have not been constrained very well and vary by over two orders of magnitude (10^{-4} – $10^{-6} M_{\odot} \text{ yr}^{-1}$; see van Loon et al. 2005; Mauron & Josselin 2011). The mass-loss rate adopted for the progenitor of SN 2020jfo in MESA is five times the typical

mass-loss rates for a RSG progenitor, but is well within the observed limits. It is difficult to predict what could have caused such a high mass-loss rate, whether it was solely due to the rotation and high-metallicity environment, or due to other factors such as interaction with a binary companion or multiple episodes of enhanced mass loss.

It was shown by Eldridge et al. (2018) that the initial progenitor masses around 8 – $15 M_{\odot}$ in the binary scenario possibly give light curves with shorter plateaus of the order of tens of days. However, their physical parameter space was limited, and not much could be said quantitatively about the progenitor properties. Another attempt by Hiramatsu et al. (2021a) showed that the RSG progenitors with initial masses of 18 – $25 M_{\odot}$ with enhanced mass-loss rates could reproduce shorter duration plateaus. However, the observed properties, viz. nebular spectra, the mass of synthesized radioactive nickel, and evolution velocities of the events (SN 2006Y, SN 2006ai, and SN 2016egz), were also supportive of higher-mass progenitors. Both these studies had shown a continuous population of Type IIP–IIL–IIb events, wherein a higher progenitor mass leads to an increased amount of stripping of the hydrogen envelope. However, SN 2020jfo poses a question to the standard progenitor scenario. The arguments presented in our analysis and discussion weigh in on a low-mass progenitor with enhanced mass loss that gave birth to the short-plateau SN, SN 2020jfo.

6. Summary

In this work, we presented an extensive multiband photometric and optical spectroscopic study of a short-plateau Type II event, namely SN 2020jfo.

1. We estimated a plateau duration of < 65 days for SN 2020jfo, putting it under the category of the rare, short-plateau Type IIP SNe.
2. The observational properties associated with SN 2020jfo are as follows: peak V -band absolute magnitude of $M_V = -17.4 \pm 0.4$ mag, peak optical luminosity of $4.3 \pm 1.4 \times 10^{42} \text{ erg s}^{-1}$, and a synthesized ^{56}Ni mass of $0.033 \pm 0.006 M_{\odot}$.
3. Using nebular-phase spectrum, we estimated a progenitor of mass $\sim 12 M_{\odot}$.
4. We estimated the progenitor properties for SN 2020jfo from hydrodynamical modeling and concluded that the most plausible progenitor is a RSG with an initial mass around $12 M_{\odot}$, radius $\sim 679 R_{\odot}$ and a final pre-SN mass $< 6.6 M_{\odot}$. It evolved in a relatively high-metallicity environment and shredded a significant amount of mass during its course of evolution.
5. A high Ni/Fe ratio of 0.18 ± 0.04 by mass was estimated for SN 2020jfo that is consistent with a low-mass progenitor ($M_{\text{ZAMS}} \leq 13 M_{\odot}$).
6. The evolution of pEW values of Fe II 5018 Å are much higher than the other Type II SNe, confirming the presence of a high-metallicity environment and a compact progenitor.
7. The presence of ionized He II line, HV $H\alpha$ feature, higher luminosity in contrast to slower velocity evolution, and the steeper decline in luminosity indicated the presence of CSM, which was confirmed by MESA+STELLA hydrodynamical modeling. It was deduced that a $0.2 M_{\odot}$ CSM, extended to a region of ~ 40 au around the progenitor,

was required to explain the early higher luminosity and a faster decline of the bolometric light curve.


We thank the referee for a thorough evaluation of the manuscript that helped in improving it. We thank the staff of IAO, Hanle, and CREST, Hosakote, that made these observations possible. The facilities at IAO and CREST are operated by the Indian Institute of Astrophysics, Bangalore. R.S.T. acknowledges Anirban Dutta for helpful discussions during this work. N.A.J. would like to acknowledge DST-INSPIRE Faculty Fellowship (IFA20- PH-259) for supporting this research. This research has made use of the High Performance Computing (HPC) resources¹¹ made available by the Computer Center of the Indian Institute of Astrophysics, Bangalore. This research made use of REDPIPE¹² (Singh 2021), an assemblage of data reduction and analysis scripts written by A.S. This research is also based on observations obtained at the 3.6 m Devasthal Optical Telescope (DOT), which is a National Facility run and managed by Aryabhata Research Institute of Observational Sciences (ARIES), an autonomous Institute under the Department of Science and Technology, Government of India. This research has also made use of the NASA/IPAC Extragalactic Database (NED¹³), which is funded by the National Aeronautics and Space Administration and operated by the California Institute of Technology. We used the Open Supernova Catalog¹⁴ (OSC; Guillochon et al. 2017) to retrieve all the light curve and spectral data for comparison. We also acknowledge Wiazmann Interactive Supernova data REpository¹⁵ (WISeREP; Yaron & Gal-Yam 2012) for spectral data downloads. This research also made use of TARDIS, a community-developed software package for spectral synthesis in supernovae (Kerzendorf & Sim 2014). The development of TARDIS received support from GitHub, the Google Summer of Code initiative, and from ESA's Summer of Code in Space program. TARDIS is a fiscally sponsored project of NumFOCUS. TARDIS makes extensive use of Astropy and Pyne.

Facilities: HCT: 2 m, Swift (UVOT), Palomar-ZTF, DOT: 3.6 m.

Software: MESA (release 15140), STELLA, PyRAF (v2.1.14), Astropy (Astropy Collaboration et al. 2018), emcee (Foreman-Mackey et al. 2013), matplotlib (Hunter 2007), pandas (McKinney 2010), SciPy (Virtanen et al. 2020), seaborn (Waskom 2021).

ORCID iDs

Rishabh Singh Teja  <https://orcid.org/0000-0002-0525-0872>

Avinash Singh  <https://orcid.org/0000-0003-2091-622X>

G. C. Anupama  <https://orcid.org/0000-0003-3533-7183>

Brajesh Kumar  <https://orcid.org/0000-0001-7225-2475>

Nayana A. J.  <https://orcid.org/0000-0002-8070-5400>

References

- Ahumada, R., Prieto, C. A., Almeida, A., et al. 2020, *ApJS*, 249, 3
 Anderson, J. P. 2019, *A&A*, 628, A7
 Anderson, J. P., González-Gaitán, S., Hamuy, M., et al. 2014, *ApJ*, 786, 67
 Andrews, J. E., Sand, D. J., Valenti, S., et al. 2019, *ApJ*, 885, 43

¹¹ <https://www.iip.res.in/?q=facilities/computing/nova>

¹² <https://github.com/sPaMFouR/RedPipe>

¹³ <https://ned.ipac.caltech.edu>

¹⁴ <https://sne.space>

¹⁵ <https://wiserep.weizmann.ac.il>

- Angulo, C. 1999, in AIP Conf. Ser. 495, Experimental Nuclear Physics in Europe: Facing the next millennium, 365
 Arcavi, I. 2017, in Handbook of Supernovae, ed. A. W. Alsabti & P. Murdin (New York: Springer International), 239
 Arnett, W. D. 1980, *ApJ*, 237, 541
 Arnett, W. D., & Fu, A. 1989, *ApJ*, 340, 396
 Asplund, M., Grevesse, N., & Jacques Sauval, A. 2006, *NuPhA*, 777, 1
 Astropy Collaboration, Price-Whelan, A. M., Sipőcz, B. M., et al. 2018, *AJ*, 156, 123
 Baklanov, P. V., Blinnikov, S. I., & Pavlyuk, N. N. 2005, *AstL*, 31, 429
 Barbon, R., Benetti, S., Cappellaro, E., Rosino, L., & Turatto, M. 1990, *A&A*, 237, 79
 Bellm, E. C., Kulkarni, S. R., Graham, M. J., et al. 2019, *PASP*, 131, 018002
 Bessell, M. S., Castelli, F., & Plez, B. 1998, *A&A*, 333, 231
 Blinnikov, S., & Sorokina, E. 2004, *Ap&SS*, 290, 13
 Blinnikov, S. I., Röpke, F. K., Sorokina, E. I., et al. 2006, *A&A*, 453, 229
 Blondin, S., & Tonry, J. L. 2007, *ApJ*, 666, 1024
 Bose, S., & Kumar, B. 2014, *ApJ*, 782, 98
 Bottinelli, L., Gouguenheim, L., Paturel, G., & de Vaucouleurs, G. 1984, *A&AS*, 56, 381
 Branch, D., & Wheeler, J. C. 2017, Type IIP Supernovae (Berlin: Springer), 245
 Brown, P. J., Holland, S. T., Immler, S., et al. 2009, *AJ*, 137, 4517
 Bruch, R. J., Gal-Yam, A., Schulze, S., et al. 2021, *ApJ*, 912, 46
 Bullivant, C., Smith, N., Williams, G. G., et al. 2018, *MNRAS*, 476, 1497
 Burrows, A., & Vartanyan, D. 2021, *Natur*, 589, 29
 Cardelli, J. A., Clayton, G. C., & Mathis, J. S. 1989, *ApJ*, 345, 245
 Chugai, N. N. 2020, *MNRAS*, 494, L86
 Chugai, N. N., Chevalier, R. A., & Utrobin, V. P. 2007, *ApJ*, 662, 1136
 Rodríguez, Ó., Clocchiatti, A., & Hamuy, M. 2014, *AJ*, 148, 107
 Curtis, S., Wolfe, N., Fröhlich, C., et al. 2020, *ApJ*, 921, 143
 Cyburt, R. H., Amthor, A. M., Ferguson, R., et al. 2010, *ApJS*, 189, 240
 Decin, L., Hony, S., de Koter, A., et al. 2006, *A&A*, 456, 549
 Dessart, L., Hillier, D. J., Waldman, R., & Livne, E. 2013, *MNRAS*, 433, 1745
 Dessart, L., Livne, E., & Waldman, R. 2010, *MNRAS*, 408, 827
 Domínguez, A., Siana, B., Henry, A. L., et al. 2013, *ApJ*, 763, 145
 Dong, Y., Valenti, S., Bostroem, K. A., et al. 2021, *ApJ*, 906, 56
 Eldridge, J. J., Xiao, L., Stanway, E. R., Rodrigues, N., & Guo, N. Y. 2018, *PASA*, 35, e049
 Elmhamdi, A., Chugai, N. N., & Danziger, I. J. 2003a, *A&A*, 404, 1077
 Elmhamdi, A., Danziger, I. J., Chugai, N., et al. 2003b, *MNRAS*, 338, 939
 Farmer, R., Fields, C. E., Petermann, I., et al. 2016, *ApJS*, 227, 22
 Filippenko, A. V. 1997, *ARA&A*, 35, 309
 Foreman-Mackey, D., Hogg, D. W., Lang, D., & Goodman, J. 2013, *PASP*, 125, 306
 Förster, F., Moriya, T. J., Maureira, J. C., et al. 2018, *NatAs*, 2, 808
 Fransson, C., & Chevalier, R. A. 1989, *ApJ*, 343, 323
 Fraser, M., Maund, J. R., Smartt, S. J., et al. 2012, *ApJL*, 759, L13
 Gehrels, N., Chincarini, G., Giommi, P., et al. 2004, *ApJ*, 611, 1005
 Glebbeek, E., Gaburov, E., de Mink, S. E., Pols, O. R., & Portegies Zwart, S. F. 2009, *A&A*, 497, 255
 Goldberg, J. A., Bildsten, L., & Paxton, B. 2019, *ApJ*, 879, 3
 Guillochon, J., Parent, J., Kelley, L. Z., & Margutti, R. 2017, *ApJ*, 835, 64
 Gutiérrez, C. P., Anderson, J. P., Hamuy, M., et al. 2014, *ApJ*, 786, L15
 Gutiérrez, C. P., Anderson, J. P., Hamuy, M., et al. 2017a, *ApJ*, 850, 90
 Gutiérrez, C. P., Anderson, J. P., Hamuy, M., et al. 2017b, *ApJ*, 850, 89
 Gutiérrez, C. P., Anderson, J. P., Sullivan, M., et al. 2018, *MNRAS*, 479, 3232
 Hamuy, M. 2003, *ApJ*, 582, 905
 Haynie, A., & Piro, A. L. 2021, *ApJ*, 910, 128
 Henyey, L., Vardya, M. S., & Bodenheimer, P. 1965, *ApJ*, 142, 841
 Hiramatsu, D., Howell, D. A., Moriya, T. J., et al. 2021a, *ApJ*, 913, 55
 Hiramatsu, D., Howell, D. A., Van Dyk, S. D., et al. 2021b, *NatAs*, 5, 903
 Huang, F., Wang, X. F., Hosseinzadeh, G., et al. 2018, *MNRAS*, 475, 3959
 Hunter, J. D. 2007, *CSE*, 9, 90
 Jacobson-Galán, W., Dessart, L., Jones, D., et al. 2022, *ApJ*, 924, 15
 Jacobson-Galán, W. V., Dessart, L., Jones, D. O., et al. 2022, *ApJ*, 924, 15
 Janka, H.-T. 2012, *ARNPS*, 62, 407
 Jerkstrand, A., Smartt, S. J., Fraser, M., et al. 2014, *MNRAS*, 439, 3694
 Jerkstrand, A., Smartt, S. J., Sollerman, J., et al. 2015b, *MNRAS*, 448, 2482
 Jerkstrand, A., Timmes, F. X., Magkotsios, G., et al. 2015a, *ApJ*, 807, 110
 Jester, S., Schneider, D. P., Richards, G. T., et al. 2005, *AJ*, 130, 873
 Kerzendorf, W. E., & Sim, S. A. 2014, *MNRAS*, 440, 387
 Maguire, K., Jerkstrand, A., Smartt, S. J., et al. 2012, *MNRAS*, 420, 3451
 Maund, J. R., Fraser, M., Smartt, S. J., et al. 2013, *MNRAS*, 431, L102
 Maun, N., & Josselin, E. 2011, *A&A*, 526, A156
 McKinney, W. 2010, in Proc. of the 9th Python in Science Conf. 56, ed. S. van der Walt & J. Millman (Austin, TX: SciPy),

- Minkowski, R. 1941, *PASP*, **53**, 224
- Moriya, T., Tominaga, N., Blinnikov, S. I., Baklanov, P. V., & Sorokina, E. I. 2011, *MNRAS*, **415**, 199
- Morozova, V., Piro, A. L., & Valenti, S. 2018, *ApJ*, **858**, 15
- Nagao, T., Maeda, K., & Ouchi, R. 2020, *MNRAS*, **497**, 5395
- Nagy, A. P., & Vinkó, J. 2016, *A&A*, **589**, A53
- Nicholl, M. 2018, *RNAAS*, **2**, 230
- Nordin, J., Brinnel, V., Giomi, M., et al. 2020, *TNSTR*, **2020-1248**, 1
- Nugis, T., & Lamers, H. J. G. L. M. 2000, *A&A*, **360**, 227
- Omar, A., Kumar, T. S., Krishna Reddy, B., Pant, J., & Mahto, M. 2019, arXiv:1902.05857
- Patat, F., Cappellaro, E., Danziger, J., et al. 2001, *ApJ*, **555**, 900
- Paxton, B., Bildsten, L., Dotter, A., et al. 2011, *ApJS*, **192**, 3
- Paxton, B., Cantiello, M., Arras, P., et al. 2013, *ApJS*, **208**, 4
- Paxton, B., Marchant, P., Schwab, J., et al. 2015, *ApJS*, **220**, 15
- Paxton, B., Schwab, J., Bauer, E. B., et al. 2018, *ApJS*, **234**, 34
- Paxton, B., Smolec, R., Schwab, J., et al. 2019, *ApJS*, **243**, 10
- Perley, D., Barbarino, C., Sollerman, J., et al. 2020, *TNSCR*, **2020-1259**, 1
- Pettini, M., & Pagel, B. E. J. 2004, *MNRAS*, **348**, L59
- Rodríguez, Ó., Pignata, G., Anderson, J. P., et al. 2020, *MNRAS*, **494**, 5882
- Poole, T. S., Breeveld, A. A., Page, M. J., et al. 2008, *MNRAS*, **383**, 627
- Poznanski, D., Prochaska, J. X., & Bloom, J. S. 2012, *MNRAS*, **426**, 1465
- Prabhu, T. P. 2014, *PINSA*, **80**, 887
- Quimby, R. M., Wheeler, J. C., Hoflich, P., et al. 2007, *ApJ*, **666**, 1093
- Roming, P. W. A., Kennedy, T. E., Mason, K. O., et al. 2005, *SSRv*, **120**, 95
- Rui, L., Wang, X., Mo, J., et al. 2019, *MNRAS*, **485**, 1990
- Sagar, R., Kumar, B., & Omar, A. 2019, *CSci*, **117**, 365
- Sahu, D. K., Anupama, G. C., Srividya, S., & Muneer, S. 2006, *MNRAS*, **372**, 1315
- Sánchez-Sáez, P., Reyes, I., Valenzuela, C., et al. 2021, *AJ*, **161**, 141
- Sanders, N. E., Soderberg, A. M., Gezari, S., et al. 2015, *ApJ*, **799**, 208
- Schlafly, E. F., & Finkbeiner, D. P. 2011, *ApJ*, **737**, 103
- Singh, A. 2021, RedPipe: Reduction Pipeline, Astrophysics Source Code Library, ascl:2106.024
- Singh, A., Kumar, B., Moriya, T. J., et al. 2019, *ApJ*, **882**, 68
- Singh, A., Srivastav, S., Kumar, B., Anupama, G. C., & Sahu, D. K. 2018a, *MNRAS*, **480**, 2475
- Singh, M., Misra, K., Sahu, D. K., et al. 2018b, *MNRAS*, **474**, 2551
- Sollerman, J., Yang, S., Schulze, S., et al. 2021, *A&A*, **655**, A105
- Sparks, W. B. 1994, *ApJ*, **433**, 19
- Srinivasaragavan, G. P., Sfaradi, I., Jencson, J., et al. 2021, arXiv:2109.02159
- Steer, I. 2020, *AJ*, **160**, 199
- Sukhbold, T., Ertl, T., Woosley, S. E., Brown, J. M., & Janka, H. T. 2016, *ApJ*, **821**, 38
- Szalai, T., Vinkó, J., Könyves-Tóth, R., et al. 2019, *ApJ*, **876**, 19
- Terreran, G., Jerkstrand, A., Benetti, S., et al. 2016, *MNRAS*, **462**, 137
- Turatto, M., Mazzali, P. A., Young, T. R., et al. 1998, *ApJL*, **498**, L129
- Valenti, S., Howell, D. A., Stritzinger, M. D., et al. 2016, *MNRAS*, **459**, 3939
- Valenti, S., Sand, D., Pastorello, A., et al. 2014, *MNRAS*, **438**, L101
- Valenti, S., Sand, D., Stritzinger, M., et al. 2015, *MNRAS*, **448**, 2608
- Van Dyk, S. D. 2017, *RSPTA*, **375**, 20160277
- Van Dyk, S. D., Cenko, S. B., Poznanski, D., et al. 2012, *ApJ*, **756**, 131
- Van Dyk, S. D., Zheng, W., Maund, J. R., et al. 2019, *ApJ*, **875**, 136
- van Loon, J. T., Marshall, J. R., & Zijlstra, A. A. 2005, *A&A*, **442**, 597
- Vink, J. S., de Koter, A., & Lamers, H. J. G. L. M. 2001, *A&A*, **369**, 574
- Virtanen, P., Gommers, R., Oliphant, T. E., et al. 2020, *NatMe*, **17**, 261
- Vogl, C., Sim, S. A., Noebauer, U. M., Kerzendorf, W. E., & Hillebrandt, W. 2019, *A&A*, **621**, A29
- Waskom, M. L. 2021, *JOSS*, **6**, 3021
- Weiler, K. W., Sramek, R. A., Panagia, N., van der Hulst, J. M., & Salvati, M. 1986, *ApJ*, **301**, 790
- Yaron, O., & Gal-Yam, A. 2012, *PASP*, **124**, 668
- Zhang, X., Wang, X., Sai, H., et al. 2022, *MNRAS*, **509**, 2013